

# The observation of Extensive Air Showers from an Earth-Orbiting Satellite

M. Pallavicini<sup>a</sup>, R. Pesce<sup>a,\*</sup>, A. Petrolini<sup>a</sup>, A. Thea<sup>a,1</sup>

<sup>a</sup>*Dipartimento di Fisica dell'Università di Genova and INFN, via Dodecaneso 33, I-16146 Genova, Italy.*

---

## Abstract

We review the main issues that are relevant for the observation of Extensive Air Showers from an Earth-Orbiting Satellite. Extensive Air Showers are produced by the interaction of Ultra-High Energy Cosmic Particles with the atmosphere and can be observed by an orbiting telescope detecting the air scintillation light.

We provide the main analytical formulas and semi-analytical results needed to optimize the design of a suitable telescope and estimate the best-expected performance and the minimal necessary requirements for the observation.

While we have in mind an EUSO-like general-purpose experiment, the results presented in this paper are useful for any kind of space-based experiment.

*Key words:* cosmic radiation; extensive air showers; space detectors; airwatch; ultra-high energy cosmic rays; ultra-high energy cosmic particles.

PACS 95.55Vj 95.55Fw

---

## 1. Introduction

Ultra-High Energy Cosmic Particles (UHECP), with energies in excess of  $E \approx 10^{19}$  eV, hit the Earth with an extremely low flux of about one particle  $\cdot \text{km}^{-2} \cdot \text{sr}^{-1} \cdot \text{millennium}^{-1}$ , for energies above  $E \approx 10^{20}$  eV [1].

The observation of UHECP and the interpretation of the related phenomenology is one of the most interesting topics of contemporary High-Energy Astro-Particle Physics. Direct detection is impossible at these energies, due to the exceedingly low flux, but UHECP can be detected by observing the Extensive Air Showers (EAS) produced by the interaction of the primary particle with the Earth at-

mosphere. For recent reviews on these topics see [2] and references therein.

Two ground-based experiments, the Pierre Auger Observatory (PAO) [3] and the Telescope Array (TA) [4], are currently taking data and hope to provide a clear understanding of many important topics in the next few years [1,5,6]. Using an hybrid detection technique, PAO and TA will improve on the results collected in the past by HiRes [7] and AGASA [8]. However, it is likely that the next generation of experiments, after PAO and TA, will use an Earth-orbiting satellite, in order to increase the event statistics, by exploiting the huge instantaneous geometrical aperture potentially available to such an experiment.

The aim of this paper is to discuss and summarize a few key issues relevant to the design and optimization of space-based experiments for the observation of UHECP. Analytical formulas and semi-analytical results will be presented and discussed, in order to

---

\* Corresponding author. Address: Dipartimento di Fisica dell'Università di Genova and INFN, via Dodecaneso 33, I-16146 Genova, Italy. E-mail: Roberto.Pesce@ge.infn.it

<sup>1</sup> Now at Eidgenössische Technische Hochschule (ETH), Zürich.

define the main parameters for the observation of EAS from space. We also summarize and update the most important results presented in [9], where more details can be found. A preliminary study was carried on in [10], which was the starting point for some of the results presented in this paper. Although the results presented in this paper refer to an EUSO-like general-purpose experiment, most of them can be applied or easily re-adapted to any space-based experiment for the observation of EAS.

The design of a telescope for the detection of EAS from space is a very challenging task, because of the low expected rate of events, the faint signal received from any EAS, the harsh space environment and the tight technical constraints imposed on a space experiment (mainly on mass, power, volume and telemetry). The engineering is very complex and the design has a strong impact on the scientific performance. A careful design optimization is therefore mandatory.

Some of the assumptions of this paper are somewhat optimistic with respect to the real conditions of the experiment, in order to be able to derive analytical formulas and semi-analytical results. We will neglect, for instance, the effect of clouds, of Mie scattering, of multiple scattering and of different types of background other than the random night-glow background; imperfections of a real apparatus will not be taken into account as well. In fact none of these effects can be easily described in a semi-analytical way. More precise and detailed results, based on more realistic conditions, can be only obtained by means of a full Monte-Carlo simulation of a specific experimental design: see the complementary paper [11]. Therefore the results of this paper are the minimal necessary requirements for the observation, but possibly not sufficient ones.

The results presented in this paper are a basic input to the detailed optimization and design of the telescope. These results cannot replace a full Monte-Carlo simulation, for detailed studies of any specific experiment. However they are extremely useful for a basic understanding, for defining a baseline design and for a rough cross-check of the results of detailed Monte-Carlo simulations. Therefore they provide a valuable starting point preliminary to any full Monte-Carlo simulation, as the latter requires a well-defined design.

Most of the work presented in this paper is the result of the development of the EUSO experiment [12], a mission of the European Space Agency (ESA), which successfully completed its phase A study in 2004 and was frozen due to programmatic

and financial reasons. The EUSO Collaboration developed a full Monte-Carlo simulation, ESAF [11], generating detailed prediction for an EUSO-like telescope.

The optimization of the design of such a challenging experiment requires to collect as many as possible preliminary information. It is the opinion of the authors that a number of preliminary and preparatory steps are mandatory [13]. The most important one is a detailed characterization of the background via a suitable micro-satellite mission [14], which might also test some of the technological issues.

The outline of the paper is as follows: the science case is briefly summarized in Section 2; the observational approach is presented in Section 3; the scientific requirements and the requirements derived for the experimental apparatus are presented in Section 4; the assumptions are summarized in Section 5; the design and optimization of an EUSO-like experiment are discussed in Section 6.

## 2. The scientific case

The present knowledge of the the physics of UHECP is still largely incomplete.

The sources and the identity of the primary particles are not known. Whether there is an end or not of the high-energy spectrum is not known either. The sources are most probably extragalactic ones and relatively nearby, but they have not been identified, yet [5,6]. The existence of a cut-off in the energy spectrum seems to be confirmed [1], but this is in agreement with a composition of the primary particles mostly consisting of protons, while data at lower energies show that the mass of the primary particles increases with the energy [5].

PAO and TA are collecting a large statistics of UHECP and starting to answer some of the open questions. However, a more complete understanding would require a systematic study of UHECP at energies above  $\approx 55$  EeV, where ground-based experiments suffer from the limited statistics. In fact, at these high energies there exist only a few measurements of the longitudinal profile of EAS, since the PAO detects and measures the longitudinal profile of about two events per year, over a total of about twenty-five events observed per year. With this limited statistics it is currently impossible to identify the sources of UHECP and to determine the primary particle identity.

A more detailed discussion of the scientific case for an UHECP space experiment can be found in [15].

### 3. The observational approach (AirWatch)

John Linsley, in 1982, first suggested [16] that the Earth atmosphere at night, viewed from space, can act as a huge calorimeter for remotely observing EAS (SOCRAS). Since then a number of proposals and studies were carried on, including the OWL [17] (Orbiting Wide-angle Light-collectors) project, the TUS/KLYPVE [18] project and EUSO [12].

In more recent times, the JEM-EUSO [19] Collaboration aims to propose again the EUSO concept on the International Space Station. The sEUSO mission [20,15,21], for a challenging next-generation experiment, was proposed to the ESA Cosmic Vision program 2015-2025 [22] and has been recommended by ESA for technological developments.

A telescope on an Earth-orbiting satellite, observing down the Earth at night <sup>2</sup>, can detect the near-UV air scintillation light isotropically produced during the EAS development in the atmosphere by the interaction of the EAS secondary particles with the air molecules. The measurement of the isotropic air scintillation light traces the development profile of the EAS. Additional information can be gathered by observing the Cherenkov light diffusely reflected by the Earth surface (by land, sea or clouds). The Earth atmosphere plays the role of a gigantic passive calorimeter, continuously changing and only usable at night. In fact the emitted light is proportional to the energy of the EAS.

This approach is complementary to ground-based observations. In fact any EAS develops close to the Earth surface and, thanks to the large distance from the EAS, a large Field of View (FoV) space-based telescope can observe a large atmospheric target. However, due to the large distance from the EAS, the light signal is definitely much fainter than the light signal observed by a ground-based experiment for the same EAS. Space-based observation is therefore best suited for observing low fluxes of high-energy UHECP.

The required telescope is an Earth-watching large aperture, large FoV, fast and highly pixelized digital camera for detecting a moving spot of near-UV single photons superimposed on a large background, designed to operate in space five years, at least.

<sup>2</sup> The term *space-based* will be used in this paper to refer to such an experiment, as opposed to the term *ground-based*.

The EAS is seen as a quasi point-like image moving on the focal surface of the telescope with a direction and an angular velocity depending on the EAS primary direction with respect to the line-of-sight. The space-time and intensity characteristics of the EAS signal is used to distinguish the EAS from various types of background (see Section 6.12), because the latter, typically, have a different space-time development.

The observational approach is schematically shown in Figure 1.

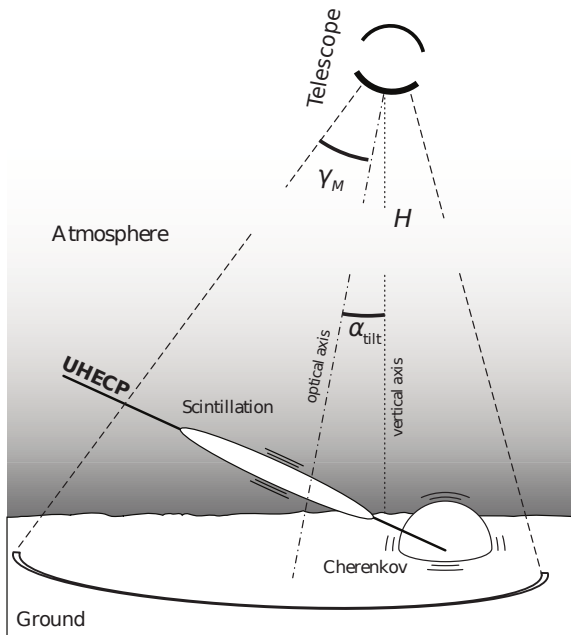


Figure 1. AirWatch observational approach:  $H$  is the orbital height,  $\gamma_M$  is the FoV half-angle and  $\alpha_{\text{tilt}}$  is the tilt angle between the optical axis and the local nadir.

An typical example of an EAS detected on the focal surface of a realistic EUSO-like telescope is shown in Figures 2 and 3.

### 4. Scientific and experimental requirements

The following scientific objectives are used in this paper, as for a general-purpose experiment: they provide the guidelines to derive the scientific requirements for the experiment.

The measured UHECP energy spectrum has to be extended beyond  $E \approx 1 \cdot 10^{20}$  eV. A map of the arrival directions of UHECP over the whole sky is required in order to identify and localize compact sources, possibly studying their energy spectra. The mass composition of the primary particles has to be

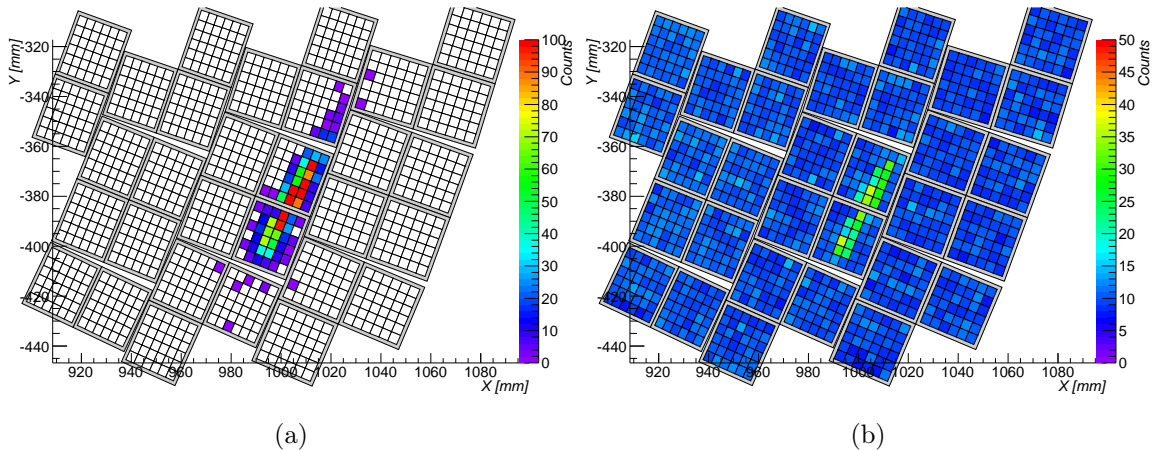


Figure 2. Image of a typical simulated  $E = 10^{20}$  eV proton EAS as seen on the focal surface of a typical  $D = 4$  m diameter space-based telescope at an altitude of 400 km above the sea level; the EAS zenith angle is  $45^\circ$ . (a) EAS signal integrated in time ( $158 \mu\text{s}$ ); the pixels without signal are in white and the PMT border is drawn in grey; (b) the background is superimposed, but only the maximum number of counts in a pixel per time unit is shown. The images are produced with ESAF [11].

measured. The ultra-high energy neutrino flux has to be measured.

From these scientific objectives, a set of scientific requirements for the experiment can be derived, see for instance [20,15].

#### 4.1. Scientific requirements

The following typical scientific requirements for UHECP observation from space are used (see also [20,15]), derived from the scientific objectives.

Of course, different scientific objectives might be conceived, possibly leading to different scientific requirements and different experiment design. The relations discussed in the rest of this paper may be adapted to the specific situations.

All sky coverage is required.

The angular resolution on the reconstructed primary UHECP direction should be  $\Delta\beta \lesssim 3^\circ$  for a large enough sub-sample of events, in order to allow the identification of compact sources while taking into account the deviation induced by magnetic fields on charged particles.

An energy resolution  $\Delta E/E \lesssim 0.3$  (including statistical and systematic contributions) is required. In fact, the energy measurement errors distort the shape of a steeply falling energy spectrum, because each energy bin collects more mismeasured EAS from low energies than it does from higher energies. A resolution smaller than  $\Delta E/E \lesssim 0.3$  does not significantly modifies the energy-spectrum shape and does not smear the GZK feature [23].

The resolution on the depth of the EAS maximum measurement has to be  $\Delta X_M \lesssim 50 \text{ g/cm}^2$  (accounting for the intrinsic variability of the EAS, depending on the UHECP primary mass).

An energy threshold  $E_{\text{TH}} \approx 1 \cdot 10^{19}$  eV is required, with a flat efficiency energy plateau at  $E \gtrsim E_{\text{TH}}$ , in order to keep systematic effects well under control. In fact, near the low-energy threshold, the total EAS detection efficiency steeply changes. This would lead to large systematic uncertainties due to the poor knowledge of the total EAS detection efficiency, which is determined from Monte-Carlo simulations only. A threshold at  $E \approx 1 \cdot 10^{19}$  eV also ensures a fair overlap with the energy spectrum observed by ground-based experiments. Furthermore the telescope must be able to measure EAS with energies up to  $E_{\text{MAX}} \approx 10^{21}$  eV, in order to study the UHECP energy spectrum in the trans-GZK region, by exploiting the larger statistics with respect to ground experiments.

The instantaneous geometrical aperture,  $\mathcal{A}_g$ , is required to be one order of magnitude larger than currently existing and/or planned ground-based experiments, in order to increase by the same amount the number of collected events:  $\mathcal{A}_g \gtrsim 10^6 \text{ km}^2 \cdot \text{sr}$ .

#### 4.2. Requirements for the experiment

##### 4.2.1. Architecture of the telescope

The required experimental telescope is made of a main digital camera, with cylindrical symmetry around the optical axis, operating in the near-UV.

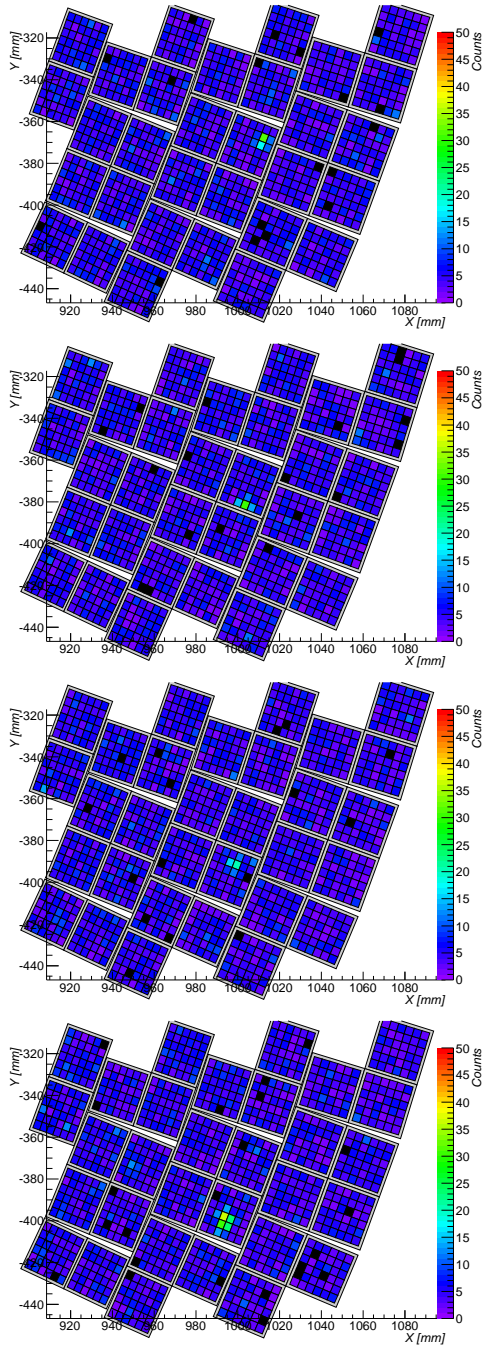


Figure 3. Image of the same EAS of Figure 2 with the background simulated. From top to bottom, the image at four different times ( $70 \mu\text{s}$ ,  $100 \mu\text{s}$ ,  $115 \mu\text{s}$ ,  $133 \mu\text{s}$ ) is shown. The off pixels are in black and the PMT border is drawn in grey. The images are produced with ESAF [11].

The digital camera must have a large aperture, a large FoV and a fast and pixelized single photon detector; the latter consists of the main optics, possibly a deployable optics, and the photo-detector on

the focal surface of the main optics.

The main optics is made of the main mirror/lenses (large, lightweight and possibly segmented), corrector mirrors/lenses, the optical filters, the active control mechanism and the supporting structure.

The photo-detector is located at the focal surface of the main optics which is typically a strongly curved surface, due to the large FoV of the optics. It is made of a bi-dimensional array of photo-sensors, the light-collection system on the photo-sensor, the front-end electronics chip and ancillary electronics, the housing, the back-end, trigger and on-board data-handling electronics.

Other ancillary systems, such as an Atmospheric Monitoring System and the Monitoring, Alignment and Self-Calibration system [24] are present.

#### 4.2.2. Mission requirements

The telescope has to observe the largest possible mass of atmosphere, with a large enough geometrical acceptance.

Obstructions of the large FoV, coming from the satellite structure, and parasitic lights coming from any other source than the EAS have to be minimized.

The orbit should be accurately designed, in order to maximize the instantaneous geometrical aperture, compatibly with the required energy threshold (see Section 6.1).

The pointing accuracy is not a critical factor provided the absolute direction of the telescope axis is known for off-line use. The pointing direction must be known off-line to within a precision of  $\lesssim 0.5^\circ$ , less than the expected angular resolution of the telescope.

The expected rate of EAS and background triggered events, affecting telemetry and telecommanding, will depend on the final orbit and therefore a precise estimation is currently lacking. It will depend on the purity of the triggered sample, which is hardly estimable without preliminary measurements.

The required lifetime is five years at least, in order to get a statistically significant sample of events, at least one order of magnitude larger than expected from ground-based experiments.

#### 4.2.3. Requirements for the telescope

The telescope will operate in single-photon detection mode in the wavelength range (WR) between 330 nm and 400 nm, to detect the air scintillation

light. Shorter wavelengths suffer absorption from the ozone layer. At higher wavelengths the scintillation emission is not significant and, moreover, the larger the wavelength range the more difficult is to design an optics free from chromatic aberrations.

The faint signal requires high photon collection area and high photon detection efficiency, as well as low noise. Small cross-talk and after-pulse rates are required in order to obtain a good energy resolution.

The dynamic range of the photo-detector should cover two orders of magnitude in signal intensity, for an effective EAS detection between  $E_{\text{TH}}$  and  $E_{\text{MAX}}$ .

The telescope should have an efficient and selective trigger system, to achieve a good background rejection on-board, and a powerful on-board data handling system as the telemetry would be limited.

The telescope has to be completely modular to reduce the risk of single point failures. Furthermore it should be robust against intense light sources like lightnings and man-made lights.

The telescope has to satisfy the constraints relevant for a space mission including mass, power, volume, telemetry, as well as the many environmental factors.

#### 4.2.4. Other technical requirements

The interior of the telescope should be light-tight such that the parasitic lights impinging onto the photo-detector will be two orders of magnitude less than the expected night-glow background rate not to worsen the energy resolution.

Other technical requirements, such as mechanical, thermal and electrical, are also important, but they are not relevant to the current discussion. See [24] for details.

## 5. Definitions and assumptions

In this section the assumptions used in the paper are introduced. The study is based on a typical hadronic EAS viewed by a simple telescope, looking downward the Earth, whose configuration and characteristics will be defined in the rest of the paper.

### 5.1. Some geometry definitions

The EAS properties depend, to a first approximation, only on the primary particle identity, its energy  $E$  and its zenith angle,  $\theta$ .

The features of the EAS image on the focal surface of the photo-detector also depend on the location of

the EAS image inside the FoV of the telescope, as defined by the angle between the optical axis and the line-of-sight,  $\gamma$ , and by the azimuth angle of the EAS image projected at the Earth surface (see Figure 4). The angle  $\gamma$  will be called, in short, *field-angle* in the rest of this paper, since it represents the visual angle inside the FoV. Whenever the optical axis is coincident with the local nadir,  $\gamma$  is coincident with the zenith angle of the line-of-sight direction. The angle between the latter and the radial direction inside the FoV is called  $\psi_a$ . If  $\varphi$  is the EAS direction azimuth angle, with respect to a global reference system  $Oxyz$ , and  $\phi$  is the azimuth angle of the line-of-sight in the FoV, then  $\psi_a = \varphi - \phi$ .

The unit vectors of the EAS direction,  $\hat{n}$ , and of the line-of-sight,  $\hat{s}$ , in the frame  $Oxyz$  are respectively:

$$\begin{aligned}\hat{n} &= \{-\sin\theta \cos\varphi, -\sin\theta \sin\varphi, -\cos\theta\} \quad , \\ \hat{s} &= \{\sin\gamma \cos\phi, \sin\gamma \sin\phi, -\cos\gamma\} \quad .\end{aligned}$$

If  $\beta$  is the angle between the EAS direction  $\hat{n}$  and line-of-sight  $\hat{s}$  from the telescope to the actual EAS location one has:

$$\cos(\beta) = \cos(\gamma) \cos(\theta) - \cos(\psi_a) \sin(\gamma) \sin(\theta) \quad . \quad (1)$$

### 5.2. Reference conditions and general assumptions

In this paper, unless otherwise specified, the conditions and parameters summarized in Table 1 will be used as a reference for most calculations.

Several assumptions, discussed in detail in this section, are used. Some of these assumptions are somewhat optimistic with respect to the real conditions of the experiment.

It is therefore emphasized once more that the results are minimal necessary, but possibly not sufficient, requirements for observation of EAS from a space-based telescope.

#### 5.2.1. Satellite parameters

The main parameters of the satellite are: its altitude above the Earth,  $H$ , (or, in more general terms, all the orbital parameters); the tilt angle  $\alpha_{\text{tilt}}$  between the optical axis and the local nadir (see Figure 1). The orbital height  $H$  is 400 km  $\lesssim H \lesssim$  1000 km (see Section 6.1).

The telescope optical axis is parallel to the local nadir, that is  $\alpha_{\text{tilt}} = 0$ . Note that, if  $\alpha_{\text{tilt}} \neq 0$ , the

Variable	Reference value	Other values
Energy	$E = 10^{19}$ eV	
Particle type	proton	
Zenith angle	$\theta = 50^\circ$	$\theta = 30^\circ, 70^\circ$
Azimuth angle	$\psi_a = 90^\circ$	$\psi_a = 0^\circ, 180^\circ$
Telescope Orbital Height [km]	$H = 700$	$H = 400, 1000$
FoV aperture (half-angle)	$\gamma_M = 20^\circ$	$\gamma_M = 15^\circ, 25^\circ$
Field-angle of observation	$\gamma = 15^\circ$	$\gamma = 10^\circ, 20^\circ$
Telescope Tilt Angle	$\alpha_{\text{tilt}} = 0^\circ$	
Total photo-detection efficiency	$\varepsilon_{\text{PD}} = 0.1$	
Operating Wavelength Range (WR) [nm]	$330 \leq \lambda \leq 400$	
Random Night-glow Background in the WR [ $\text{ph} \cdot \text{m}^{-2} \text{s}^{-1} \text{sr}^{-1}$ ]	$B = 5 \cdot 10^{11}$	$B = (0.3 \div 1.0) \cdot 10^{12}$

Table 1  
Parameters and conditions used as reference.

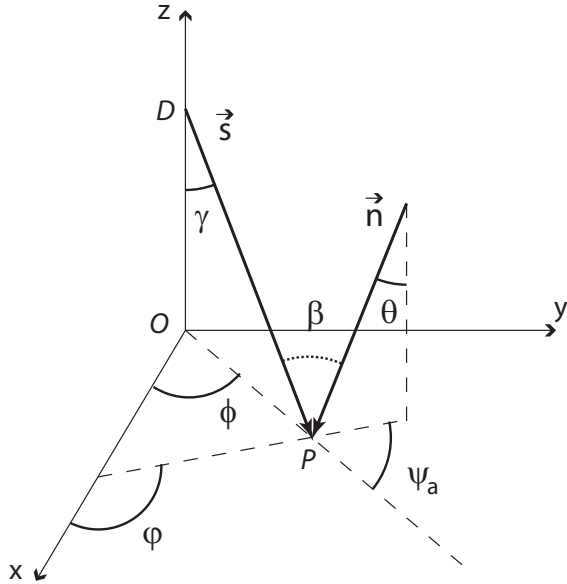


Figure 4. Definition of the angles with respect to a global coordinate frame  $Oxyz$ , in the case of no tilt between the direction of the local nadir and the optical axis. The  $D$  is the position of the telescope,  $O$  is the telescope nadir and  $P$  is the impact point of the EAS on the Earth surface. The EAS direction is  $\mathbf{n}$  (zenith angle  $\theta$  and azimuth angle  $\varphi$ );  $\mathbf{s}$  the direction of the line-of-sight (zenith angle  $\gamma$  and azimuth angle  $\phi$ );  $\beta$  is the angle between  $\mathbf{n}$  and  $\mathbf{s}$ , while  $\psi_a = \varphi - \phi$ .

line-of-sight zenith angle is different from the field-angle  $\gamma$ .

### 5.2.2. EAS image properties

Any EAS, when observed from space, can be geometrically modeled as a point moving on a straight line at the speed of light. It therefore produces, on

the curved focal surface of the photo-detector, an image generated by a point moving on a line.

A reference energy  $E = 1 \cdot 10^{19}$  eV is used (Table 1), corresponding to the required energy threshold. In fact the higher the energy of the EAS, the better it can be reconstructed, as more photons are detected.

The EAS direction and  $\psi_a$  strongly affect the kinematics of the EAS image and therefore its observability and its observed features. For several reasons, to be discussed later, only EAS with a zenith angle  $30^\circ \lesssim \theta \lesssim 70^\circ$  will be studied, with a reference zenith angle  $\theta = 50^\circ$ . In fact a very inclined EAS cannot be easily studied in a semi-analytical way, as it gives a very long image on the focal surface, such that the curvature and the changes of the photo-detection characteristics of the focal surface cannot be neglected. On the other hand, an almost vertical EAS produces a very short image on the focal surface and it is therefore hard to reconstruct the EAS. In order to describe an average behavior a reference angle  $\psi_a = \pm 90^\circ$  will be used.

Note that, when observing from space, up-going EAS could be observed, with  $\theta > 90^\circ$ .

### 5.2.3. Atmospheric profiles

The Linsley's parametrization of the US Standard Atmosphere [25] is used. This parametrization can be sometimes approximated with the simpler exponential density profile (isothermal atmosphere) as a function of the altitude,  $h$ , above the sea level [26]:

$$\rho(h) = \rho_0 e^{-h/h_0} \quad (2)$$

with  $h_0 = 8.4$  km,  $\rho_0 = 1.2249$  kg/m<sup>3</sup>.

#### 5.2.4. Sphericity of the Earth

A spherical Earth with radius  $R_{\oplus} = 6371$  km is used. The exact relation between the altitude above the Earth surface,  $h$ , and the distance  $\ell$  measured along a straight line with zenith angle  $\theta$  is:

$$\frac{d\ell}{dh} = \frac{h + R_{\oplus}}{\sqrt{h^2 + 2R_{\oplus}h + R_{\oplus}^2 \cos^2 \theta}} \quad (3)$$

$$\approx \left(1 - \frac{h}{R_{\oplus}} \tan^2 \theta\right) \sec \theta \quad .$$

In the approximation of flat Earth, when  $h \tan^2 \theta \ll R_{\oplus}$ , the relation between  $h$  and  $\ell$  becomes:

$$\frac{d\ell}{dh} = \sec \theta \quad . \quad (4)$$

It is also worth remembering the definition of the slant depth,  $X$ :

$$\frac{dX}{d\ell} = \rho \quad , \quad (5)$$

plus the appropriate boundary condition on  $X$  at some  $\ell$ .

#### 5.2.5. EAS longitudinal and lateral profile

The Gaisser-Hillas parametrization [27,28] of an hadron-induced EAS describes the EAS longitudinal profile as a gamma distribution:

$$N_{\text{ch}}(X) = N_{\text{M}}^{\text{ch}} \left(\frac{X - X_0}{X_{\text{R}}}\right)^{X_{\text{R}}/\Lambda} e^{-(X_{\text{R}} + X_0 - X)/\Lambda}$$

for  $X \geq X_0$  ,

(6)

where  $N_{\text{ch}}(X)$ , the number of charged particles at the slant depth  $X$ , is expressed in terms of:  $N_{\text{M}}^{\text{ch}}$ , the number of charged particles at the EAS maximum;  $X_{\text{M}}$ , the depth of the EAS maximum;  $X_0$ , a fitting parameter;  $X_{\text{R}} \equiv X_{\text{M}} - X_0$  and  $\Lambda \simeq 65$  g/cm<sup>2</sup>, the interaction mean free path. This expression makes explicit the invariance of the EAS longitudinal profile with respect to shifts of the parameter  $X_0$ .  $X_0$  is often set at the first interaction point, although it is only a fitting parameter and it can also take negative values. The  $\Lambda$  parameter is rather energy independent and very similar for both proton and

iron induced EAS in the energy range under study. Finally  $N_{\text{M}}^{\text{ch}} \approx \kappa E$ , with  $\kappa \simeq 0.6/\text{GeV}$  [29].

Typical values for  $X_{\text{M}}$  and  $X_0$  at  $E = 10^{19}$  eV are given in Table 2, inferred from Monte-Carlo simulations done with CONEX [30].

Parameter	Proton	Iron
$N_{\text{M}}^{\text{ch}}$	$6 \cdot 10^9$	$6 \cdot 10^9$
$\Lambda$	$65$ g/cm <sup>2</sup>	$65$ g/cm <sup>2</sup>
$X_{\text{M}}$	$790 \pm 40$ g/cm <sup>2</sup>	$700 \pm 30$ g/cm <sup>2</sup>
$X_0$	$35 \pm 5$ g/cm <sup>2</sup>	$10 \pm 2$ g/cm <sup>2</sup>
$X_{\text{R}}$	$755 \pm 45$ g/cm <sup>2</sup>	$690 \pm 42$ g/cm <sup>2</sup>

Table 2

Typical Gaisser-Hillas parameters of a  $E = 10^{19}$  eV EAS for both proton and iron primaries.

A parameter strictly related to  $X_{\text{M}}$  is the altitude of the EAS maximum,  $h_{\text{M}}$ , which is fundamental for the reconstruction of  $X_{\text{M}}$  itself. It depends on  $X_{\text{M}}$  through the EAS zenith angle  $\theta$  and the atmospheric density profile. The values of  $h_{\text{M}}$ , as a function of  $\theta$ , are shown in Figure 5 for three different  $X_{\text{M}}$  using the Linsley's parametrization of the atmosphere density profile. The exponential (isothermal) profile for  $X_{\text{M}} = 800$  g/cm<sup>2</sup> is also shown for comparison: it is clear that the choice of the atmosphere density profile does not strongly affect  $h_{\text{M}}$  up to  $\theta \approx 70^\circ$ .

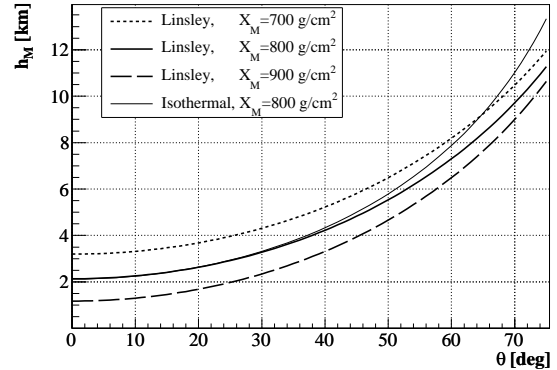


Figure 5. The altitude of the EAS maximum versus the EAS zenith angle for various atmospheric profiles.

The lateral EAS profile is not accounted for in this study, as it is hardly accessible when observing from space. Indeed, the typical EAS lateral size is of about one km, corresponding to the required spatial granularity (see Section 6). The EAS image is therefore only one or two pixels wide (for a perfect optics).



### 5.2.6. Length of the EAS track

A typical hadronic EAS of  $E \approx 10^{19}$  eV with  $\theta \lesssim 70^\circ$  is seen on the focal surface of the telescope as a few degrees long track, as discussed in detail in Section 6.7. This value is easily estimated by computing the EAS length between the first interaction point and the ground. The real length on the focal surface of the telescope is even shorter, due to the predominance of background with respect to signal at the beginning of the EAS.

Within this short angular interval any possible change of the focal surface detection properties can therefore be neglected. Obviously this would not be true for a very inclined EAS ( $\theta \gtrsim 70^\circ$ ), which may appear many degrees long and cannot be easily described in a simple parametrized form.

### 5.2.7. Random Background

The background in the observation of EAS from space is very complex and produced by many sources (see Section 6.12 for more details).

Only the random background due to the atmospheric night-glow and to the moon and starlight has been taken into account, as it can be easily modeled. A uniform, isotropic and constant background, on the space-time scale of the EAS development is used. A reference value for the background of  $B \approx 0.5_{-0.2}^{+0.5} \cdot 10^{12}$  photons  $\cdot$  m $^{-2}$ s $^{-1}$ sr $^{-1}$  [31], in the wavelength range WR, is used. The available measurements give, under certain circumstances, a value up to a factor two larger, depending on the conditions (including moon phases and cloudiness) [31].

This random background, gives a large rate with respect to a typical EAS signal, and must be coped with (see Section 6.12). In this study it is assumed that the underlying background can be subtracted away, in real time at the trigger level, in the region nearby the EAS, by continuously measuring the average photon rate on a pixel-by-pixel basis. This is an optimistic but mandatory requirement to deal with the large random background.

The expected large rate implies a small relative error on the background estimate (see Appendix A.4). An appropriate statistical estimator to compare signal to background is therefore  $S/\sqrt{B}$ .

### 5.2.8. Air scintillation yield

The EAS develops in the atmosphere at an altitude  $h \lesssim 20$  km (see Figure 5). In this part of atmosphere the air scintillation yield in the wavelength range WR can be considered as nearly con-

stant [32], roughly equal to  $Y \simeq (4.2 \pm 0.2)$  photons  $\cdot$  particle $^{-1}$  m $^{-1}$ . Whenever a better precision is required the yield measurements of [33,34,35] are used.

### 5.2.9. Atmospheric transmission

The atmospheric transmission is naively modeled taking into account Rayleigh scattering only. In fact Mie scattering is more important at low altitudes of a few km, while the EAS predominantly develops above a few km of altitude (see Figure 5). Mie scattering is therefore ignored in this study at the current level of approximation, as we are studying the minimal necessary requirements for observation.

The atmospheric transmission as a function of the zenith angle  $\chi$ , when taking into account Rayleigh scattering only, can be roughly parametrized as:

$$T_a(\chi, h) \approx \exp \left[ - \left( \frac{\rho_0 h_0}{\Lambda_R(\lambda)} \right) M(h, \chi) \exp \left( - \frac{h}{h_0} \right) \right] \quad (7)$$

$$\text{with } \frac{\rho_0 h_0}{\Lambda_R} \approx 0.7 \quad \text{for } \lambda = 337 \text{ nm} \quad ,$$

where:  $h_0$  and  $\rho_0$  are, respectively, the atmosphere scale height and the atmospheric density at the sea level (see equation (2));  $\Lambda_R(\lambda)$  is the Rayleigh mean free path at the wavelength  $\lambda$  [36];  $M(h, \chi)$  is the air-mass function at the zenith angle  $\chi$  [37]. When taking into account the Earth curvature, the air-mass is given by the Chapman function  $\text{Ch}(h, \chi)$  [38].

Table 3 shows the ratio,  $\mathcal{R}$ , between the atmospheric transmission for a zenith angle  $\chi$  and the same quantity along the vertical direction for different altitudes. The table shows that at  $\chi \gtrsim 80^\circ$  the atmospheric transmission from ground to infinity is reduced by more than one order of magnitude with respect to the vertical. This is crucial to evaluate of the effectiveness of a tilting of the telescope with respect to the nadir direction, as it will be discussed later (Section 6.8.4).

The atmospheric geodesic refraction is usually negligible. In fact the correction for the refraction when observing an object at the Earth surface from a height  $H$ , at a zenith angle  $\chi$  with respect to the nadir, is  $\Delta\chi \approx 62.37'' \tan \chi$ , for  $\chi \lesssim 80^\circ$  at a wavelength  $\lambda = 337$  nm [26]. This implies  $\Delta\chi \approx 0.008^\circ$  at  $\chi = \gamma_M = 25^\circ$ . The effect of the refraction is therefore small with respect to the angular pixel size, typically of  $\sim 0.1^\circ$  (see Section 6). However, the effect of atmospheric refraction might be important for a tilted telescope, when observing at large angles

$\chi$	$\mathcal{R}(h = 0 \text{ km})$	$\mathcal{R}(h = 5 \text{ km})$	$\mathcal{R}(h = 10 \text{ km})$
0°	1.000	1.000	1.000
10°	0.989	0.994	0.997
20°	0.956	0.976	0.986
30°	0.897	0.942	0.968
40°	0.808	0.889	0.937
50°	0.679	0.808	0.889
60°	0.499	0.682	0.810
70°	0.265	0.481	0.668
80°	0.042	0.173	0.380
90°	$6.4 \cdot 10^{-11}$	$2.4 \cdot 10^{-6}$	$7.9 \cdot 10^{-4}$

Table 3

Ratio  $\mathcal{R} \equiv T_a(\chi, h)/T_a(\chi = 0, h)$  between the atmospheric transmission from the altitude  $h$  above the ground to the telescope (at infinity), for a zenith angle  $\chi$  and the same quantity for  $\chi = 0^\circ$ , for three different altitudes. All the quantities are evaluated for a wavelength  $\lambda = 337 \text{ nm}$  using equation (7).

with respect to nadir: at  $\chi = 80^\circ$  (maximum zenith angle with a tilt  $\alpha_{\text{tilt}} \approx 60^\circ$ ), it is  $\Delta\chi \approx 0.1^\circ$  [26].

As we are studying the minimal necessary requirements for observation, we will neglect multiple scattering and the effects of clouds, which are important in a real experiment. In fact these effects are difficult to study without a full Monte-Carlo simulation and a precise experimental design. Clear sky conditions are used. See [11,39,40] for studies of the effects of clouds.

## 6. Concept design and optimization of the experiment

In this section the requirements on the telescope, derived from the scientific requirements, will be presented and discussed in detail.

### 6.1. Orbit

The choice of the orbit of the telescope is a trade off between the energy threshold and the observed atmosphere volume.

The orbital height,  $H$ , (defined as the semi-major axis of an elliptical orbit) is one of the most important parameters. In fact a higher altitude provides a larger instantaneous geometrical aperture, but also a higher energy threshold because of the smaller EAS signal received by the telescope.

Practical and technical constraints may limit the orbital parameters. Indeed, orbits lower than about

300 km height suffer too much atmospheric drag and require frequent re-boosts. On the other hand, orbits higher than about 1000 km height are difficult to manage because the radiation environment undergoes a substantial change due to the presence of Van Allen belts, whose high level of trapped radiation may adversely affect the satellite operation.

An orbit with a variable  $H$  is useful in order to extend the range of energy of the observed EAS: a satellite on an elliptic orbit spends more time at higher altitudes, gaining in the instantaneous geometrical aperture, but it also spends some time at lower altitudes, decreasing the energy threshold for EAS observation, in an energy range where a long observation time might be not necessary, as the UHECP flux at lower energy is larger.

An orbit in the range of heights between  $H_{\text{MIN}} \approx 400 \text{ km}$  and  $H_{\text{MAX}} \approx 1000 \text{ km}$  would scale up/down both the UHECP energy range and the instantaneous geometrical aperture by a factor:  $(H_{\text{MAX}}/H_{\text{MIN}})^2 \approx 6$ . On the other hand, linear distances, affecting the angular resolution and pixel size, only scale as  $H$ , and not as  $H^2$  (see Section A.3).

The orbital height might be also varied by using different almost circular orbits during the mission lifetime (for example part of the time at a lower altitude and part of the time at a higher altitude). Natural orbit decay might be exploited as well.

The orbit lifetime depends on the orbital height and it strongly depends on the epoch of the Solar cycle (that is on the epoch of the Mission), which affects the atmospheric density (see Figure 6).

Another key parameter to keep in mind is the ballistic coefficient of the satellite, defined as  $m/(C_d A_{\text{sat}})$ , where  $m$  is the satellite mass,  $A_{\text{sat}}$  is its cross-sectional area and  $C_d \approx 2.2$  is the atmospheric drag coefficient). It is expected to be rather low, due to the large expected area-to-mass ratio and therefore the atmospheric drag is expected to be large.

Another important parameter is the *observational duty cycle*, defined as the fraction of time with the telescope taking data. The orbit design must be further optimized to avoid as much as possible the light pollution from man-made sources at ground, from lightnings (mainly present on the land in the equatorial regions), from auroras and other parasitic light sources. The effects of a short duty cycle can be recovered, in principle, by increasing the mission lifetime.

The orbit can be also optimized to fly over spe-

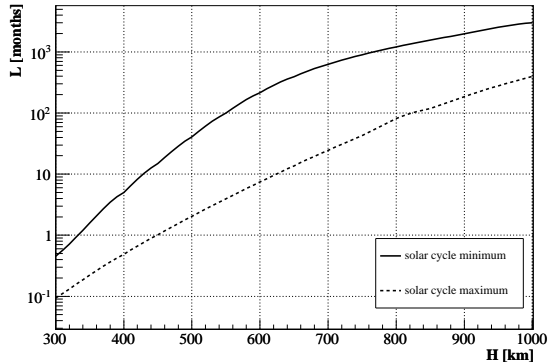


Figure 6. Lifetime  $L$  (in months) of a satellite (mass  $\sim 3000$  kg; cross-sectional area  $\sim 150$  m<sup>2</sup>) versus the orbital height  $H$ . Formulae and data for calculation can be found in [41].

cific fixed targets at ground, as often as possible. Such targets include ground-based EAS experiments, weather stations and ground-based calibration sources. In particular, observations above ground-based EAS experiments, namely the Pierre Auger Observatory and Telescope Array, might be useful for cross-calibration.

The coincidence rate of events detectable both by a space-based and a ground-based experiment, strongly depends on the orbit. Order of magnitude estimates give the following results, taking a duty cycle of about 13% for the space-based experiment (an hybrid ground-based experiment has a duty cycle very close to 1). In case of one passage per orbit above the ground target one has about 5/15 events/year above 10/5 EeV, in coincidence with the PAO, and about 1/3 events/year above 10/5 EeV, in coincidence with the TA. In the case of a random passages above the ground target, these numbers go down to 0.1/0.4 events/year for the PAO and 0.03/0.1 events/year for the TA.

In fact, by designing a specific trigger only operational during the passages above the ground target, all the data collected by the telescope could be kept for offline analysis.

Clearly the design of the orbit is a crucial issue for such an experiment. It is therefore preferred an experiment based on a free-flyer, whose orbit can be optimized, to same extent, than an experiment, for instance, on the International Space Station.

## 6.2. Optical system

The two basic optical parameters, affecting both the performance and the engineering of the experi-

ment, are the Entrance Pupil (EP) area,  $A_{EP}$ , and the FoV-angle  $\gamma_M$ , defined as half the opening angle of the circular cone generating the FoV of the optics (see Figure 1).

The large required entrance pupil (a few meters diameter) calls for a ratio between the focal length and the entrance pupil diameter as small as possible, in order to reduce the size of the focal surface (see Section 6.2.4).

### 6.2.1. Entrance pupil of the optics

The entrance pupil area,  $A_{EP}$ , or, equivalently, its diameter (also called *optics aperture*),  $D_{EP}$ , is the basic parameter that affects the telescope sensitivity to low intensity signals. Increasing the optics aperture, to within the external and practical constraints, provides a guaranteed improvement of the telescope performance, since the number of detected photons increases.

The optics aperture also determines the size of the telescope and, consequently, the mass and the volume of the payload of the satellite. For large entrance pupil diameters ( $\gtrsim 3$  m), a deployable optics is most probably required to fit within the space launch vehicle.

The total number of detected photons is roughly proportional to the solid angle subtended by the optics entrance pupil as seen by the EAS ( $\Omega \approx A_{EP}/H^2$ ).

The minimum value for  $A_{EP}$  is basically set by the requirement on the energy threshold, while the upper limit is fixed by practical constraints such as money and technological readiness. As the telescope is basically photon-limited, the entrance pupil must be as large as possible.

In order to reach an energy threshold as low as  $E_{TH} \approx 10^{19}$  eV, an entrance pupil diameter of the order of few meters at an orbital height between 400 km and 700 km is required, (see Section A.2).

### 6.2.2. FoV of the optics

In order to increase the instantaneous geometrical aperture (Section 6.8) and the number of detected EAS, either a higher orbit or a tilt of the telescope with respect to nadir might be more effective than increasing the FoV. Indeed these two options might have two beneficial effects: keep the focal surface size limited and ensure a better optics performance, as the performance of any optics becomes typically worse when the FoV increases.

The tight constraints of any space mission require the optical system to be simple (few light-weight components). Such an optics has typically a relatively large Point Spread Function (PSF), which varies with the position on the focal surface. The size and shape of the PSF has a direct impact on the spatial resolution at ground and the signal to background ratio. Therefore its optimization over the focal surface is one of the critical aspects of the optical system design. It is worthwhile to mention that a PSF much smaller than the required resolution on ground would not be a realistic option, as the necessary number of pixels would become too large. The optimal telescope design combines a sufficiently small PSF, and a pixel size of similar magnitude, to limit the number of pixels.

In the present discussion, a FoV aperture (half-angle)  $15^\circ \leq \gamma_M \leq 25^\circ$ , coming from the requirements on the instantaneous geometric aperture (see Section 6.8), is used.

### 6.2.3. Reflective optics versus refractive optics

One main drawback of a reflective system is that the center of curvature of the focal surface is on the opposite side with respect to the incoming light. The filling of the focal surface with the array of photo-sensors is therefore more difficult and the filling factor is worse than for a refractive system, with the center of curvature of the focal surface is on the same side with respect to the incoming light. Furthermore a reflective system would suffer from the obscuration due to the focal surface and the very limited room for the photo-detector. The latter might be a real issue, depending on the kind of photo-sensors adopted.

On the other hand, a refractive system is possibly difficult to deploy and a complex supporting structure is required due to its large dimensions, causing some obscuration. As for ground-based astronomical telescopes, it is unpractical and difficult to build refractive telescopes above a certain size: an entrance pupil diameter of a few meters is larger than the largest ground-based refractive astronomical telescope.

On the basis of contemporary technology, a reflective system seems to be a more viable option than a refractive one.

### 6.2.4. Size of the Focal Surface

To a first approximation, the diameter of the focal surface,  $D_{PD}$ , is a function of the FoV-angle  $\gamma_M$  and

of the focal length  $f$ :

$$D_{PD} \approx 2f \sin \gamma_M \quad . \quad (8)$$

Introducing the optics  $f$ -number:

$$F_n \equiv f/D_{EP} \quad , \quad (9)$$

where  $D_{EP}$  is the diameter of the entrance pupil, the above equation can be re-written as:

$$D_{PD} \approx 2F_n D_{EP} \sin \gamma_M \quad . \quad (10)$$

Note that for  $\gamma_M = 30^\circ$  and  $F_n = 1$  the focal surface is as large as the entrance pupil.

A reasonable assumption for any real telescope is that the focal surface is not larger than the optics: if the latter is approximated by the optics entrance pupil, as it is desirable for a high-efficiency optics, this implies the rough estimate:  $2F_n \sin \gamma_M \lesssim 1$ .

A detailed discussion of these and other topics about the optics can be found in [42].

## 6.3. Effect of the observation angle

At the edge of FoV ( $\gamma \simeq \gamma_M$ ) the triggering and reconstruction of the EAS is more difficult than near the center of the FoV. In fact, due to the larger EAS distance, the flux of photons decreases as  $\approx \cos^2 \gamma$  (the *proximity factor*).

The effective entrance pupil typically decreases as  $\cos \gamma$ , for a flat entrance pupil. It is the so-called *obliquity factor* of the optics: the entrance pupil area is seen reduced by a factor  $\cos \gamma$  by incoming photons off-axis by an angle  $\gamma$ .

Combining the obliquity and the proximity factors, the number of signal photons falls as  $\cos^3 \gamma$  from pure geometrical effects.

Under realistic assumptions, the optical system design is a trade-off among the strict mass constraint, the complexity of the optics and the large required aperture and FoV. An optics with such features is likely to be affected by anisoplanatism: the PSF is optimized for a certain field angle  $\gamma_{\text{best}}$  (best focus, smallest size and almost round shape of the PSF, little glare) but at field angles other than the optimal one, aberrations appear, the type and strength of which depends on the optics implementation details. The choice of  $\gamma_{\text{best}}$  is driven by the scientific goals. If  $\gamma_{\text{best}} = 0$ , then the central region combines the best image quality with a small obliquity factor, so that a lower energy threshold is achieved. On the other hand, if  $\gamma_{\text{best}}$  is close to the

edge of the FoV, it can be used to partially compensate the worsening effects due the obliquity factor.

In order to quantify the capability to focus incoming light onto a sufficiently small region, it is useful to introduce the *optical triggering efficacy* (with dimensions of an area) as

$$\mathcal{E}'_O(\gamma) \equiv \frac{\Phi_b(\gamma)}{I(\gamma)} \quad , \quad (11)$$

where  $I(\gamma)$  is the *photon irradiance* of the signal (the number of photons per unit time per unit area perpendicular to the line of sight) and  $\Phi_b(\gamma)$  the number of photons incident on the focal surface per unit time within a pixel bucket (that is a fiducial region around the centroid of the PSF). The signal photons falling outside the pixel bucket are usually too diluted to be associated to the EAS signal, and are lost in the background, contributing to the veiling glare, especially at low energies. In the case of an ideal optics the optical triggering efficacy becomes

$$\mathcal{E}'_O(\gamma) = A_{EP} \cos \gamma \quad , \quad (12)$$

where  $\cos \gamma$  is nothing but the obliquity factor. In real optical systems the optical triggering efficacy usually decreases faster than  $\cos \gamma$ , for instance due to the absorption losses and off-axis aberrations.

An EAS detected at the edge of the FoV would also suffer from a larger atmospheric attenuation  $T_a$  (see equation (7)), due to the longer and more inclined path in the atmosphere.

Generally speaking, the FoV central region (more photons, better optical quality but smaller geometrical acceptance) is better for detecting low energy events with a low photon flux, while the regions near the edge of the FoV (less photons, worse optical quality but larger geometrical acceptance) are better for detecting high energy events with a high photon flux.

#### 6.4. The Photo-Detector on the focal surface

In this section rough basic estimates of an ideal photo-detector parameters are derived. More precise estimates, for instance to quantify the deviations from ideality, would require a full Monte-Carlo simulation and a precise design of the main optics.

As discussed in section 6.2.4, a large focal surface area of a few squared meters is required, to be filled with compact, robust and light-weight photo-sensors.

The pixel size is driven by two competing requirements: increasing  $H$  (or tilting the telescope) requires a smaller pixel size; increasing the optics aperture (and therefore the focal length) implies a larger light spot on the focal surface and therefore a larger pixel size.

The PSF of the optics has to match, approximately, the photo-detector pixel size. In fact, even though a finer pixel granularity would allow a better reconstruction, provided that enough photons are collected, a trade-off with cost and complexity is unavoidable. On the other hand a pixel size much larger than the PSF would not exploit all the quality of the optics (see section 6.9).

The desired number of pixels,  $N_{\text{pix}}$ , of the photo-detector can be estimated by the relation

$$N_{\text{pix}} \approx \frac{\pi H^2 \tan^2 \gamma}{(\Delta L)^2} \quad , \quad (13)$$

where  $\Delta L$  is the linear granularity at ground.

The required photo-detector pixel size,  $d$ , corresponding to observing a length  $\Delta L$  on the Earth surface, is then

$$d \approx \frac{f \Delta L}{H} \quad . \quad (14)$$

The photo-detector surface has to approximate the focal surface of the optics, which is expected to be strongly curved due to the large FoV and the impossibility to build an optimized optics with many components. The focal surface, to a first approximation, can be assumed to have a spherical shape (the exact shape for a spherical primary mirror), with radius equal to  $f$  and maximum angular aperture  $\gamma_M$ . Its area,  $A_{PD}$ , is given by

$$A_{PD} = 2\pi f^2 (1 - \cos \gamma_M) \quad . \quad (15)$$

The approximate maximum number of pixels which can be fitted on the focal surface of the photo-detector is

$$N_{\text{pix}} \approx \frac{A_{PD}}{d^2} \quad . \quad (16)$$

Alternatively the desired pixel size on the focal surface can be estimated, in terms of the focal surface parameters and the desired number of pixels, by the relation

$$d \approx \sqrt{\frac{A_{PD}}{N_{\text{pix}}}} \quad . \quad (17)$$

Note that, to the present level of approximation and with the present parameters, the two equations (14) and (17) are roughly equivalent, given the equations (13) and (15).

The angular granularity of the photo-detector,  $\Delta\alpha$ , is given by the relations

$$\Delta\alpha \approx \frac{\Delta L}{H} \simeq \frac{d}{f} . \quad (18)$$

The solid angle coverage of every pixel,  $\Delta\Omega$ , is given by

$$\Delta\Omega \approx \frac{(\Delta L)^2}{H^2} \simeq \frac{d^2}{f^2} \simeq [\Delta\alpha]^2 . \quad (19)$$

The optics also determines the distribution of incidence angles of the photons on the focal surface, which has some impact on the photo-detector design, because the detection efficiency of the photo-sensor in general depends on it. The marginal ray angle is determined by the  $F_n$  of the optics and is given by the relation

$$\tan \gamma_{\text{marg}} \approx \frac{1}{2F_n} , \quad (20)$$

which leads to a large spread of incidence angles of photons on the focal surface.

In order to reduce the effect of defocusing on the large and curved focal surface a good fit between the ideal focal surface of the optics and the real shape of the photo-detector must be implemented. In general it is not trivial at all to obtain a good fit, because the optimized focal surface of the optics has a complex geometrical shape while the photo-sensor modules typically have a flat photo-sensitive surface with a simple geometrical shape. The approximate maximum defocusing in the direction parallel to the focal surface,  $\Delta w$ , produced by a small displacement  $\Delta z$  in the direction perpendicular to the focal surface, is given by the relation

$$\Delta w \approx \Delta z \tan \gamma_{\text{marg}} = \frac{\Delta z}{2F_n} . \quad (21)$$

It should be  $\Delta w \ll d$ , which sets a requirement on the maximum value of  $|\Delta z|$ .

### 6.5. The detected air scintillation signal

It is worthwhile to recall the relation between the signal from the EAS detected by the telescope and the most basic parameters of the EAS, of the atmosphere and of the telescope itself. All the formulas

presented in this section depend on the photon wavelength, but the explicit dependence will be omitted.

An EAS develops at the speed of light  $c$ , starting from the first interaction point  $\mathbf{x}_0$ , along the longitudinal coordinate  $\ell = c(t - t_0) = |\mathbf{x}(t) - \mathbf{x}_0|$ , where  $\mathbf{x}(t)$  or  $\mathbf{x}(\ell(t))$  is the position as a function of time. Let  $\mathbf{x}_T$  be the position of the telescope, assumed to be constant during the EAS development.

Three main factors contribute to the number of signal counts,  $\mathcal{N}$ : the air scintillation signal  $N_{\text{sc}}$ , the atmospheric transmission from the EAS to the telescope  $T_a$  and the telescope photo-detection efficacy  $\mathcal{E}_{\text{tel}}$ , with the dimensions of an area. Let  $\Delta\ell$  be a short segment of the EAS located at  $\mathbf{x}(\ell)$ . The characteristics of the three previous factors can be taken as constant over  $\Delta\ell$  and therefore:

$$\mathcal{N} = \frac{\mathcal{E}_{\text{tel}} T_a N_{\text{sc}}}{4\pi |\mathbf{x} - \mathbf{x}_T|^2} . \quad (22)$$

The number of air scintillation photons generated by the EAS segment  $\Delta\ell$  is given by

$$N_{\text{sc}} = N_{\text{ch}}(\mathbf{x}) Y(\mathbf{x}) \Delta\ell , \quad (23)$$

where  $N_{\text{ch}}(\mathbf{x})$  is the number of charged particles in the EAS and  $Y(\mathbf{x})$  is the air scintillation yield. In principle,  $Y(\mathbf{x})$  also depends on the energy of the charged particles, which varies with the energy and zenith angle of the EAS. However, at this level of approximation, only the dependence on the spatial position will be taken into account.

The atmospheric transmission,  $T_a$ , depends on the emission point  $\mathbf{x}$  and the telescope position  $\mathbf{x}_T$ , or equivalently on the angle  $\chi$ , and the altitude of the emission point  $h(\ell)$ , see equation 7.

The overall *photo-detection efficacy* of the telescope,  $\mathcal{E}_{\text{tel}}$ , factors into the optical triggering efficacy,  $\mathcal{E}'_O$ , the optical filters efficiency,  $\varepsilon_f$ , and the overall photo-detection efficiency,  $\varepsilon_{\text{PD}}$ :

$$\mathcal{E}_{\text{tel}}(\gamma) = \mathcal{E}'_O \varepsilon_f \varepsilon_{\text{PD}} . \quad (24)$$

The overall photo-detection efficiency  $\varepsilon_{\text{PD}}(\gamma)$  is the probability that a photon reaching the photo-detector will fire the front-end electronics producing a recorded photon hit. It is one of the most important parameters affecting the performance and depends itself on many parameters, in particular on the field-angle  $\gamma$ . For instance, the incidence angle of the incoming photons at the photo-detector entrance window changes with the field-angle. Typically, the larger the incidence angle, the lower the photo-detector efficiency is. The smaller the FoV of

the optics the larger the incidence angles are, according to relation (20).

For space-qualified standard PMT, already tested in the space environment,  $\varepsilon_{\text{PD}} = 0.12 \div 0.15$ . Even in the most optimistic scenario it is not realistic to expect more than a factor three improvement of the  $\varepsilon_{\text{PD}}$  in the near future, provided that successful efforts can be devoted to the development of suitable photo-sensors with higher quantum efficiency, that is nowadays the main source of inefficiency. However also the geometrical acceptance and filling factor of the array of photo-sensors are crucial issues.

Recently new photocathodes for photo-multiplier tubes have been developed. They have a quantum efficiency about twice the one of traditional bi-alkali photo-cathodes, see for instance [43]. Moreover many different concepts of solid state photo-sensor devices are being actively developed by many research groups. These devices, which come with different names (GAPD, SiPM, ...), aim to reach a total photo-detection efficiency of  $\varepsilon_{\text{PD}} = 0.4 \div 0.6$  (see, for instance, [44] for the most recent developments). However, in order to be ready for EAS observation from space, some R/D is still required to improve on such parameters as dark count rate, filling factor and quantum efficiency in the near-UV.

Other effects may affect the overall photo-detection efficiency, with efficiencies typically very close to one. These effects include, for instance, reflection and absorption at the various optical elements, the filling factor of the focal surface with the real photo-sensor modules, threshold and pile-up effects in the front-end electronics. However the product of many efficiencies close to one can decrease the overall efficiency by a substantial amount. However, as they are already very close to one, there is little hope to gain anything substantial there.

The number of signal photons produced by a segment  $\Delta\ell$  of the EAS, at the coordinate  $\mathbf{x}$ , and detected by the telescope is thus:

$$\mathcal{N} = \frac{N_{\text{ch}} Y \Delta\ell}{4\pi |\mathbf{x} - \mathbf{x}_{\text{T}}|^2} T_{\text{a}}(\chi, h) \mathcal{E}'_{\text{O}}(\gamma) \varepsilon_{\text{f}} \varepsilon_{\text{PD}} \quad . \quad (25)$$

This equation can be used after defining the fiducial region on the focal surface such that photons are considered to be detected photons, that is photons that are close enough to the centroid of the image spot, see Section 6.3. The photons outside the fiducial region just contribute to the veiling glare, reducing the image contrast.

It is worthwhile to note that for faint signals (a few photons per pixel) the errors in the equation (25) will be typically dominated by the Poisson statistical fluctuations. In fact, for EAS with a number of detected signal photons  $\mathcal{N} \approx 100$ , less than 10 photons per pixel are expected with a relative statistical error of the order of 0.3, larger than the expected systematic errors of about 15% (see Appendix A.3).

#### 6.5.1. Multi-photon detection factors

Other more complex factors, involving multi-photon correlations on the same pixels and correlations between photons in neighboring pixels, will affect the EAS detection efficiency. These include cross-talk, the front-end/read-out electronics and trigger efficiency and the event reconstruction efficiency. These effects are very difficult to estimate without a full Monte-Carlo simulation [11,45,46], as they depend on the contribution of all the photons at once.

#### 6.5.2. Signal and background roll-off with field-angle

Let us assume an ideal optics:  $\mathcal{E}'_{\text{O}}(\gamma) = A_{\text{EP}} \cos \gamma$ .

The field-angle dependence of the signal,  $S(\gamma)$ , for a given source is given by

$$S(\gamma) \propto T_{\text{a}}(\gamma, 0) \mathcal{E}'_{\text{O}}(\gamma) \cos^2 \gamma \quad (26)$$

$$\longrightarrow \gamma(0^\circ \rightarrow 25^\circ) : (1.0 \rightarrow 0.69) \quad .$$

The field-angle dependence of the random background,  $B(\gamma)$ , is

$$B(\gamma) \propto \mathcal{E}'_{\text{O}}(\gamma) \quad (27)$$

$$\longrightarrow \gamma(0^\circ \rightarrow 25^\circ) : (1.0 \rightarrow 0.90) \quad .$$

Both signal and random background decrease at increasing field-angles, but in a different way:  $S$  decreases faster than  $B$  with  $\gamma$ . In fact the field-angle dependence of the ratio between the signal and the square root of the random background is:

$$\frac{S}{\sqrt{B}}(\gamma) \propto T_{\text{a}}(\gamma, 0) \sqrt{\mathcal{E}'_{\text{O}}(\gamma)} \cos^2 \gamma \quad (28)$$

$$\longrightarrow \gamma(0^\circ \rightarrow 25^\circ) : (1.0 \rightarrow 0.73) \quad ,$$

The dependence on the field-angle of both the signal and  $S/\sqrt{B}$  makes the increase of the optics FoV useless above a certain extent for a nadir pointing telescope. Similar considerations apply to tilted instruments (see section 6.8.4).

The trigger settings require tuning as a function of the field-angle, that is as a function of the radial distance on the focal surface.

One important result is that a detection energy threshold about two times higher is expected for events detected at  $\gamma = 25^\circ$  with respect to events detected on-axis, because the efficiency curve as a function of the energy roughly scales as the inverse number of signal photons detected [11,45,46].

### 6.6. Number of detected photons and energy resolution

The desired energy resolution ( $\Delta E/E \sim 0.2 \div 0.3$ ) calls for a relative error due to the Poisson statistics of the number of detected photons,  $\mathcal{N}$ , not larger than  $1/\sqrt{\mathcal{N}} \sim (0.10 \div 0.15)$ , assuming an equal contribution from Poisson statistical and other systematic errors. This implies that at least  $\mathcal{N} \simeq 100$  photons must be detected from any EAS at the lowest energies, with full detection efficiency. Obviously, the number of detected photons impacts significantly on all the other observables too.

The time-integrated irradiance of the signal reaching the telescope, as a function of the zenith angle  $\theta$ , is shown in the Figure 7. For an ideal optics and the reference conditions of Table 1, the required overall triggering efficacy and the minimum telescope diameter can be inferred from the time-integrated irradiance (see section A). This result does not depend on the implementation of the optical system and the photo-sensor. The required overall triggering efficacy for observing the same EAS scales as  $H^2$ .

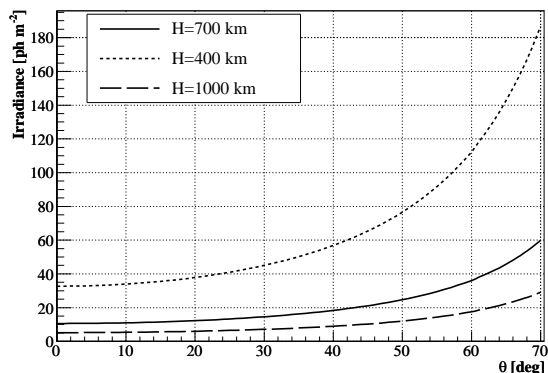


Figure 7. Signal time-integrated irradiance in the reference conditions of Table 1, as a function of  $\theta$ .

It follows that a minimum entrance pupil diameter  $D_{EP} \approx 8$  m is required to observe  $\mathcal{N} \simeq 100$  signal

photons, in the reference conditions of Table 1, at the energy threshold.

### 6.7. The length and duration of the visible EAS image

The angle subtended by the visible EAS image on the focal surface of the telescope and its time duration, which two important quantities, necessary for the experiment design, are easily estimated by determining the first and last detected points of the EAS image.

If one assumes to be able to subtract all the background and neglects the contribution of the Cherenkov light reflected by the Earth surface, the shape of the detected photon hits is well described by the Gaisser-Hillas function (equation (6)), which is a Gamma distribution in the variable  $\hat{X} \equiv X - X_0$ :

$$g(\hat{X}) = \frac{b^{-a} \hat{X}^{a-1}}{\Gamma(a)} e^{-\frac{\hat{X}}{b}} \propto \hat{X}^{\frac{X_R}{\Lambda}} e^{-\frac{\hat{X}}{\Lambda}} \quad (29)$$

where  $a \equiv \frac{X_R}{\Lambda} + 1$ ,  $b \equiv \Lambda$ ,  $X_R \equiv X_M - X_0$ .

The mean and the standard deviation of this gamma distribution are:

$$\begin{aligned} \langle \hat{X} \rangle &= ab = X_M - X_0 + \Lambda \quad , \\ \sigma_{\hat{X}} &= b\sqrt{a} = \sqrt{\Lambda(X_M - X_0 + \Lambda)} \quad . \end{aligned}$$

The number of detected photons,  $\mathcal{N}$ , can be estimated starting from the parameters of the EAS and telescope. Moreover they follow the probability distribution of equation (29). The minimum and maximum value and the range of  $\hat{X}$  (see Figure 8) as a function of  $\mathcal{N}$  can be easily determined from simulations of Gamma distributions, using the physical parameters given in section 5.2, Table 2. Simulations give good enough results for the present study; they are easier and faster than a precise analytical study (see for instance [47]). A proton primary particle was used, but it has been checked that the results do not differ significantly for other primary hadrons. For instance, in case of an iron EAS at  $E = 10^{19}$  eV, the range for  $\mathcal{N} = 100$  is  $4.9\sigma$  instead of  $5.0\sigma$ .

The minimum and maximum value and the range of  $\hat{X}$  as a function of  $\mathcal{N}$  are given in Figure 9 and Table 4. As it is required to observe  $\mathcal{N} \simeq 100$  photons at the energy threshold, the range turns out to be about  $5\sigma$ .



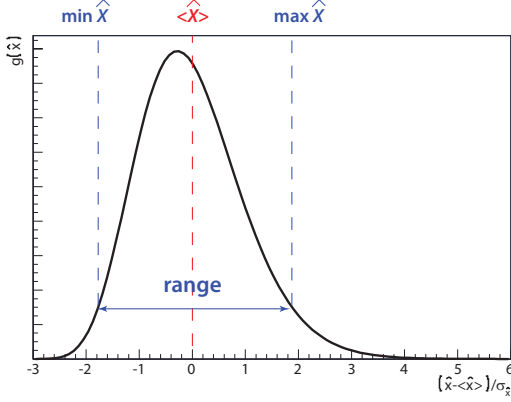


Figure 8. An example of Gamma function  $g(\hat{X})$ , with the indication of the minimum and maximum values and the range of  $\hat{X}$ .

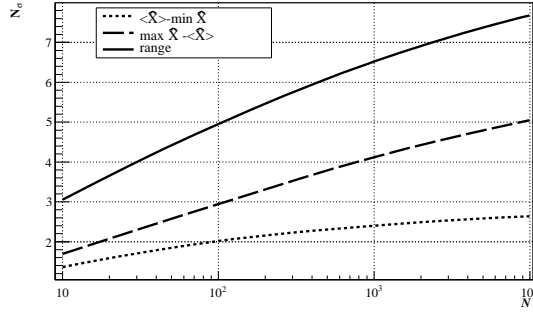


Figure 9. The minimum and maximum values and the range of  $\hat{X}$  as a function of  $\mathcal{N}$  for a Gamma distribution with parameters corresponding to the reference EAS (Table 1).

As expected, the results show that, due to the Gamma-like shape of the Gaisser-Hillas function, the range of the detected photon distribution (that is the observed image length) does not change by a large amount as a function of the number of detected photons. In fact, as Figure 9 shows, the range is roughly a logarithmic function of the number of detected photons.

$\mathcal{N}$	range	$\langle \hat{X} \rangle - \min \hat{X}$	$\max \hat{X} - \langle \hat{X} \rangle$
10	$(3.2 \pm 0.1)\sigma$	$1.4\sigma$	$1.8\sigma$
100	$(5.0 \pm 0.1)\sigma$	$2.0\sigma$	$3.0\sigma$
1000	$(6.5 \pm 0.1)\sigma$	$2.4\sigma$	$4.1\sigma$
10000	$(7.9 \pm 0.1)\sigma$	$2.6\sigma$	$5.3\sigma$

Table 4

Estimation of the range of a Gamma distribution in the reference conditions of Table 1.

From the above results, it is easy to estimate the angle  $\xi_{\text{EAS}}$  subtended by the EAS image and the

EAS image duration  $T_{\text{EAS}}$ . The dependence on the EAS zenith angle  $\theta$  of the angular extension and time duration of a  $E = 10^{19}$  eV proton EAS image are shown respectively in Figures 10÷12 for different heights of the satellite and different values of  $\psi_a$ .

The Figures show that, typically,  $\xi_{\text{EAS}} \lesssim 3^\circ$  and  $T_{\text{EAS}} \lesssim 100 \mu\text{s}$ , justifying the assumptions of section 5. Note also that, for  $\theta \lesssim 50^\circ$ , the EAS are truncated because they hit the ground, as it is shown by the cusps in the figures. Nevertheless the truncation does not affect the reference EAS (Table 1).

The time duration of the EAS image is almost independent on both  $H$  and  $\gamma$  for a fixed EAS geometry (see Figures 11(b) and 12(b)). The angular length, for the same EAS, will scale as  $\sim \cos \gamma / H$ .

Some numerical values for the reference EAS are given in section A.1. More plots can be found in [9].

## 6.8. Aperture

### 6.8.1. Area observed at the Earth

In the case of a nadir pointing telescope the geometrical area spanned by the FoV at the surface of the Earth is

$$A_0 = 2\pi R_\oplus^2 (1 - \cos \beta_M) \quad , \quad (30)$$

in terms of  $H$ , the orbital height,  $R_\oplus$ , the Earth radius,  $\gamma_M$  the half-angle FoV of the telescope, and  $\beta_M$ , the angle at Earth center between nadir and the FoV border

$$\beta_M = \arcsin \left( \frac{R_\oplus + H}{R_\oplus} \sin \gamma_M \right) - \gamma_M \quad (31)$$

The total atmosphere target mass,  $M_a$ , can be estimated from  $A_0$  using the value of the vertical column density of air ( $\sim 1033 \text{ g/cm}^2$ ). Some values are given in Table 5 for different values of  $H$  and  $\gamma_M$ .

The expression for  $A_0$  reduces, in the flat Earth approximation, to the well-known expression:

$$A_0 = \pi H^2 \tan^2 \gamma_M \quad . \quad (32)$$

### 6.8.2. Instantaneous geometrical aperture

The instantaneous geometrical aperture is defined as:

$$\mathcal{A}_g \equiv \int_A \int_\Omega \hat{n}(\theta, \varphi) \cdot \hat{k} d\Omega dA \quad , \quad (33)$$

in terms of the normalized EAS direction vector,  $\hat{n}(\theta, \varphi)$ , the normal unit vector to the Earth surface,

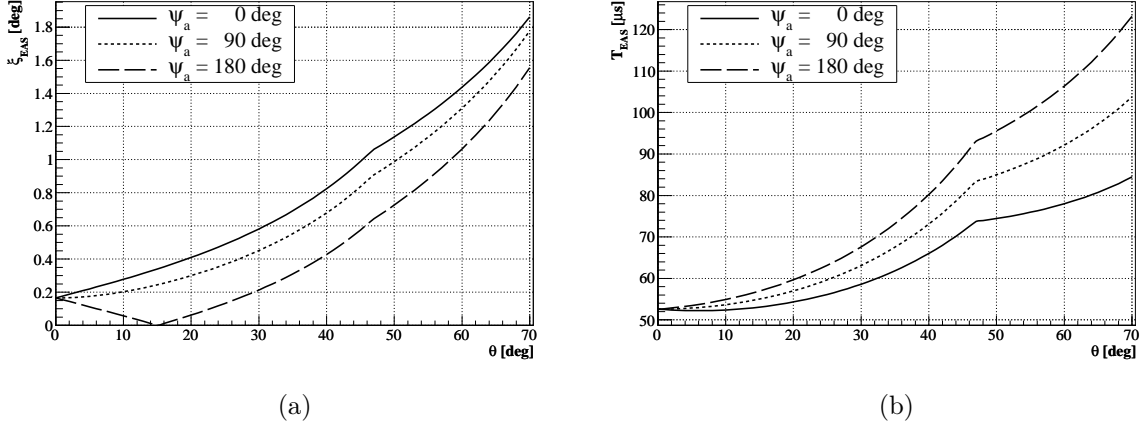


Figure 10. Angular extension (a) and time duration (b) of a  $E = 10^{19}$  eV proton EAS image as a function of  $\theta$  ( $H = 700$  km and  $\gamma = 15^\circ$ ).

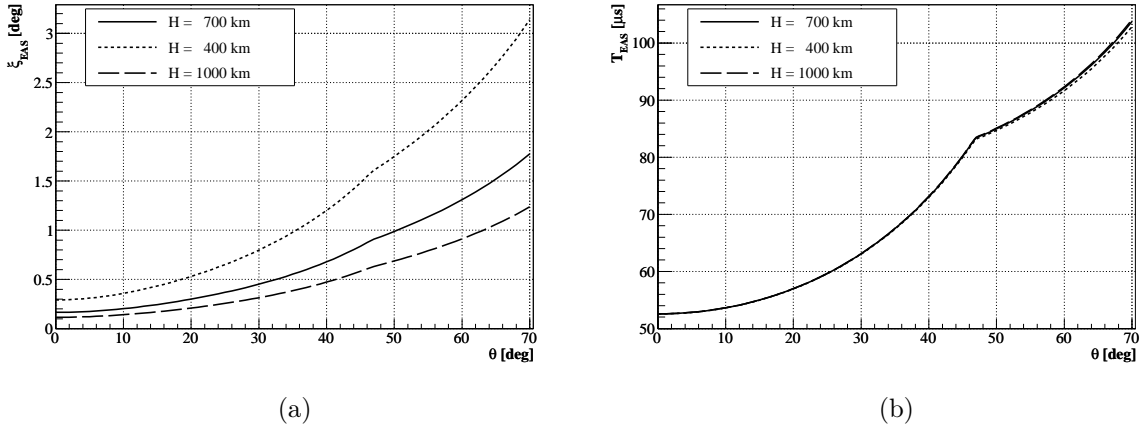


Figure 11. Angular extension (a) and time duration (b) of a  $E = 10^{19}$  eV proton EAS image as a function of  $\theta$  ( $\psi_a = 90^\circ$  and  $\gamma = 15^\circ$ ).

$H$	$\gamma_M$	$A_0$	$M_a$
		units of	units of
		[ $1 \cdot 10^5 \text{ km}^2$ ]	[ $1 \cdot 10^{15} \text{ kg}$ ]
400	20	0.67	0.7
700	20	2.07	2.1
1000	20	4.25	4.4
700	15	1.11	1.2
700	25	3.43	3.5

Table 5  
Area observed at the Earth and atmosphere mass target.

$\hat{k}$ , the target area,  $A$ , and the solid angle  $\Omega$ . For EAS with  $0 \leq \varphi \leq 2\pi$  and  $0 \leq \theta \leq \frac{\pi}{2}$ , the instantaneous geometrical aperture reduces to

$$\mathcal{A}_g = \pi A_0 \quad . \quad (34)$$

The instantaneous geometrical aperture is related to the rate of observed EAS by the relation

$$\frac{dN_{\text{events}}}{dt} = \mathcal{A}_g J(E \geq E_{\text{TH}}) \quad , \quad (35)$$

where  $J$  is the flux of primary UHECP.

Equation 34 implies that in order to reach  $\mathcal{A}_g \gtrsim 10^6 \text{ km}^2 \cdot \text{sr}$  it has to be  $\beta_M \gtrsim 2.86^\circ$ . The choice  $H = 700$  km and  $\gamma_M = 25^\circ$  satisfies this requirement.

### 6.8.3. Effective aperture

The effective aperture of a nadir pointing telescope, when considering all the EAS which reach the

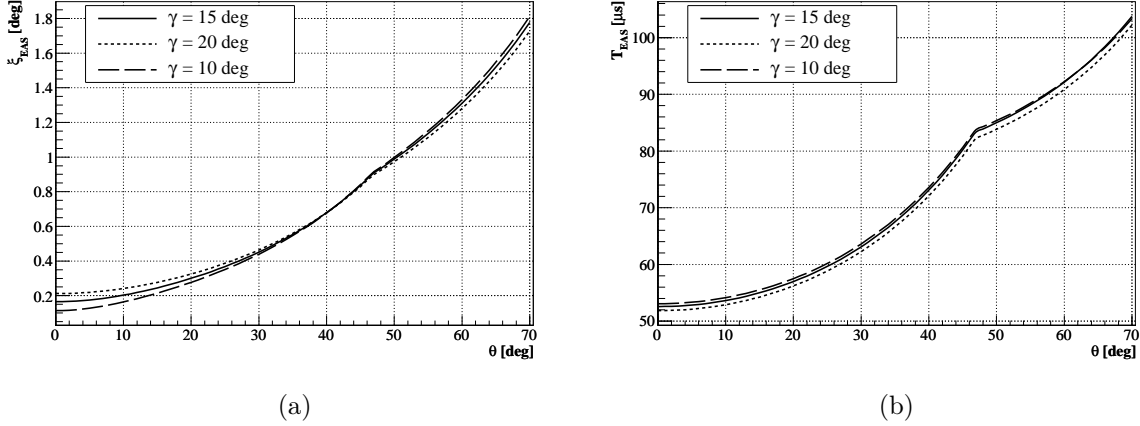


Figure 12. Angular extension of a  $E = 10^{19}$  eV proton EAS image on the focal surface as a function of  $\theta$  ( $H = 700$  km and  $\psi_a = 90^\circ$ ).

ground inside the FoV at any zenith angle, is approximately given by the relation:

$$\begin{aligned} \mathcal{A}_e &= \eta_o \eta_c (1 - \tau_{\text{dead}}) \mathcal{A}_g(\gamma_M, H) \\ &\approx 2\eta_o \eta_c (1 - \tau_{\text{dead}}) \pi^2 R_\oplus^2 (1 - \cos \beta_M) \end{aligned} \quad (36)$$

in terms of the orbital height,  $H$ , the half-angle FoV  $\gamma_M$ , the observational duty cycle  $\eta_o$ , the dead time  $\tau_{\text{dead}}$  and the factor  $\eta_c \sim 0.5$ , quantifying the effect of real cloud coverage on the EAS detection efficiency. This expression gives the asymptotic aperture, when the total detection efficiency of the EAS is equal to one.

#### 6.8.4. Tilting of the telescope

The instantaneous geometrical aperture can increase if the telescope is tilted with respect to the local nadir by some angle  $\alpha_{\text{tilt}}$ .

In this case, the geometrical solution to the problem of finding the intersection area of the circular FoV cone with the spherical Earth surface is not trivial at all. The easiest way to estimate the aperture is therefore to use a simple Monte-Carlo integration.

The Monte-Carlo results for the intersection area, as a function of  $\alpha_{\text{tilt}}$ , are shown in Figure 13 for different values of  $H$  and  $\gamma_M$ .

It should be noted that the corresponding horizon angle is

$$\beta_{\text{hor}} = \arcsin\left(\frac{R_\oplus}{R_\oplus + H}\right) \quad (37)$$

$$\approx \begin{cases} 70^\circ & \text{at } H = 400 \text{ km} \\ 64^\circ & \text{at } H = 700 \text{ km} \\ 60^\circ & \text{at } H = 1000 \text{ km} \end{cases} \quad (38)$$

which has to be taken into account when computing the maximum possible tilting angle.

The instantaneous geometrical aperture, in tilted mode, can increase up to a factor (3÷5), with respect to the case of no tilt.

The main drawback of tilting is that the atmospheric absorption increases at the far extreme of the FoV (see Table 3). This means that the effective energy threshold in the far part of the FoV increases. Moreover the FoV is non-uniform and the angular resolution at the far extreme becomes worse than at nadir. The large FoV of the optics, together with the large atmospheric target observed, would require an excellent stray-light control for a tilted telescope due to the large amount of stray light entering the FoV. Tilting, together with the large FoV, would also strongly affect the duty cycle, by a factor which cannot be easily estimated semi-analytically, as the large area observed at the Earth would more often include day-time areas and sources of stray light.

On the other hand increasing the orbit height seems to be a more effective method to increase the instantaneous geometrical aperture while minimizing the drawbacks mentioned above. In fact one would have no significant losses from the increased atmospheric transmission and a more uniform FoV. A highly elliptical orbit is also an option.

#### 6.8.5. Duty cycle

It is not easy to estimate the duty-cycle of a space-based telescope without a dedicated preliminary measurement of the real background seen from the real satellite orbit.

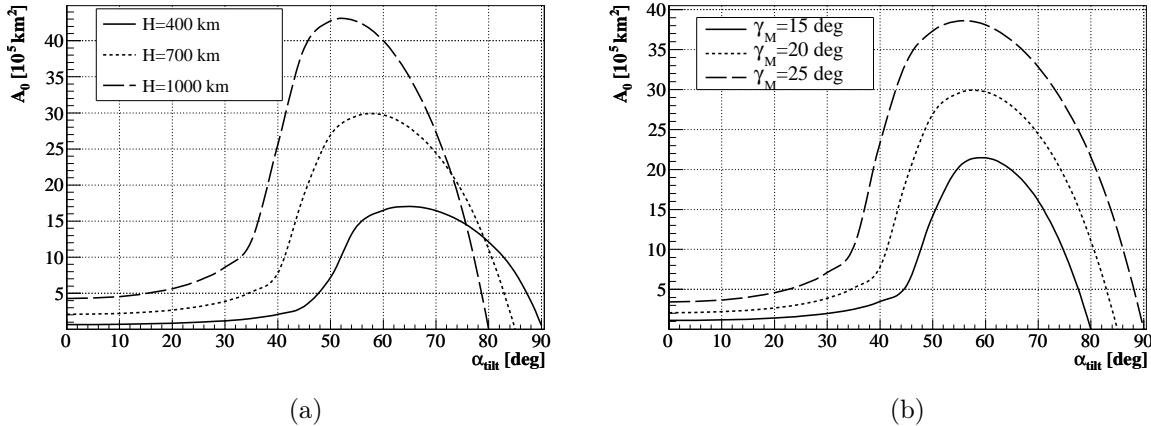


Figure 13. Observed  $A_0$  versus  $\alpha_{\text{tilt}}$ . (a): for  $\gamma_M = 20^\circ$ ; (b): for  $H = 700$  km.

The observational duty cycle is driven by the acceptable background level and it is therefore dependent on the range of energies of the EAS under study. However to allow for background dependent observations implies a very precise knowledge of the telescope sensitivity as a function of the background level.

The major limitation to the telescope observational duty cycle comes from Sun light and Moon light. The fraction of time the telescope is unable to operate depends on the orbit and, during moon-time, on the maximum background rate such that data taking, that is online background subtraction, is possible.

For an orbital height  $H \sim 400$  km, an orbit inclination of  $\sim 50^\circ$  and requiring both the Sun and the Moon to be safely below the horizon, the average estimated duty cycle is  $\eta_o \sim 13\%$ . If one accepts an additional background flux of  $B_{\text{ML}} \approx 100 \text{ ph m}^{-2} \text{ ns}^{-1} \text{ sr}^{-1}$ , due to Moon light, the estimated duty cycle is  $\eta_o \sim 19\%$  [48].

The duty cycle may be also influenced by man-made or other natural sources (see section 6.12).

### 6.9. Pixel size

The pixel size,  $\delta$ , is driven by the scientific requirements and constrained by the available technology and resources.

The number of signal photons divided by the number of random background photons on the pixel roughly scales as  $S/B \sim 1/\Delta\alpha$  (where  $\Delta\alpha$  is the angular pixel size corresponding to  $d$ , see equation (18)) for a pixel much larger than the EAS

track width on the focal surface (which basically depends on the optics PSF) while it saturates to a constant for a small enough pixel size.

The pixel size also affects the angular resolution and the  $X_M$  resolution.

Due to the relatively small EAS transverse dimensions, the width of the EAS image on the focal surface will be determined by the PSF only.

A pixel size roughly the same size of the optics PSF turns out to be, usually, a good compromise as it allows to exploit the optics performance. On the contrary, a pixel size much smaller than the optics PSF requires a much larger number of detector channels and allows to obtain a sub-pixel resolution, only in case the number of incident photons is large.

An approximate and simplified analysis, leading to determine the required pixel size starting from the angular resolution, is presented in Section 6.10.

### 6.10. Angular resolution

Any EAS will be seen as a point moving inside the FoV with a kinematics (direction and angular velocity) determined by the EAS direction relative to the line-of-sight from the telescope to the EAS instantaneous position. The direction of the EAS velocity vector, as seen by the telescope, can be decomposed into two perpendicular components: the one parallel to the line-of-sight and the other one lying in the plane perpendicular to it. The EAS develops approximately at the speed of light and its distance can be considered as a known value, in the case of a space-based experiment. Both components can be

reconstructed from the two-dimensional image on the focal surface plus the timing information.

Using the reference conditions of Table 1 and exploiting the Gamma-like shape of the EAS longitudinal profile, the relation between the observed EAS angular length,  $\xi_{\text{EAS}}$ , and the standard deviation of the observed longitudinal photon distribution along the EAS image,  $\sigma_\xi(\mathcal{N})$ , turns out to be  $\xi_{\text{EAS}} = 5\sigma_\xi$  (for  $\mathcal{N} = 100$ ), as discussed in section 6.7.

The determination of angular resolution of the two components, perpendicular and parallel to the line-of-sight, are presented respectively in Sections 6.10.1 and 6.10.2.

Note that the following elementary analysis ignores the effect of the background, which will make the angular resolution worse. On the other hand, the use of the diffusely reflected Cherenkov flash, if implemented, might improve the angular resolution.

#### 6.10.1. Angular resolution perpendicular to the line-of-sight

The expected angular resolution  $\Delta\beta_\perp$  on the EAS direction perpendicular to the line-of-sight is readily estimated by a linear fit. The error on the angle can be calculated from the standard errors relations for the least squares fit to a straight line with equal errors in both variables as [49]:

$$\Delta\beta_\perp(\mathcal{N}) = \frac{\Delta\alpha}{\sqrt{12}} \frac{1}{\sigma_\xi(\mathcal{N})} \frac{1}{\sqrt{\mathcal{N}}} \quad , \quad (39)$$

where  $\sigma_\xi(\mathcal{N} = 100) \approx \xi_{\text{EAS}}(\mathcal{N} = 100)/5$  (see Section 6.7) and  $\Delta\alpha$  is the angular pixel size.

Note that the above result is consistent with the naive evaluation:

$$\Delta\beta_\perp \approx \frac{\Delta\alpha}{\xi_{\text{EAS}}} \frac{1}{\sqrt{\mathcal{N}}} \quad . \quad (40)$$

#### 6.10.2. Angular resolution parallel to the line-of-sight

The relation between the observed angular velocity  $\omega$  and the angle  $\beta_\parallel$  between the EAS velocity vector and the line-of-sight is the well known relation [50,51]:

$$\omega = \frac{c}{D} \left( \frac{1 - \cos\beta_\parallel}{\sin\beta_\parallel} \right) = \frac{c}{D} \tan\left(\frac{\beta_\parallel}{2}\right) \quad , \quad (41)$$

where  $c$  is the speed of light and  $D$  is the distance of the EAS.

In the present case, one assumes that the EAS develops in the lower layers of the atmosphere, within

$\sim 15$  km from the ground, so that  $D$  is approximately known (the relative error is  $\Delta D/D \lesssim 0.05$ ).

The error on the angle  $\beta_\parallel$  can be estimated from the equation  $\alpha(t) = \omega t$  using the standard errors relations for the least squares fit to a straight line with equal errors in both variables as [49]:

$$\begin{aligned} \Delta\beta_\parallel(\mathcal{N}) &= \frac{K}{\sqrt{\mathcal{N}}} \frac{1}{\sqrt{\left(\frac{\sigma_t(\mathcal{N})}{\Delta\tau}\right)^2 + \left(\frac{\sigma_\xi(\mathcal{N})}{\Delta\alpha}\right)^2}} \\ &\approx \frac{1}{\sqrt{\mathcal{N}}} \frac{1}{\sqrt{\left(\frac{\sigma_t(\mathcal{N})}{\Delta\tau}\right)^2 + \left(\frac{\sigma_\xi(\mathcal{N})}{\Delta\alpha}\right)^2}} \quad , \\ K &\equiv \frac{2}{\sqrt{12}} \frac{D\Delta\alpha}{c\Delta\tau} \frac{\left[1 + \left(\frac{c\Delta\tau}{D\Delta\alpha}\right)^2 \tan^2\left(\frac{\beta_\parallel}{2}\right)\right]}{\left[1 + \tan^2\left(\frac{\beta_\parallel}{2}\right)\right]} \quad , \end{aligned} \quad (42)$$

where  $\Delta\tau$  is the time resolution of the telescope, while  $\sigma_\xi(\mathcal{N} = 100) \approx \xi_{\text{EAS}}(\mathcal{N} = 100)/5$  and  $\sigma_t(\mathcal{N} = 100) \approx T_{\text{EAS}}(\mathcal{N} = 100)/5$  (see Section 6.7) and  $\Delta\alpha$  is the angular pixel size.

#### 6.10.3. Requirements deriving from the angular resolution

In the reference conditions of Table 1, a FoV granularity of  $\Delta\alpha \sim 0.1^\circ$  is required, from equation 39, in order to reach an angular resolution of the order of  $\Delta\beta_\perp \sim 1^\circ$ . Moreover, in order to reach an angular resolution of the order of  $\Delta\beta_\parallel \sim 1^\circ$ , a time resolution  $\Delta\tau = 2.5 \mu\text{s}$  is required, from equation 42.

The above results lead to two similar values of the angular resolutions  $\Delta\beta_\perp$  and  $\Delta\beta_\parallel$ , which can be written, neglecting the soft (roughly logarithmic) dependence on  $\mathcal{N}$  of  $\sigma_\xi$  and  $\sigma_t$ , as:

$$\Delta\beta_\perp(\mathcal{N}) \approx \frac{0.14}{\sqrt{\mathcal{N}}} \quad \Delta\beta_\parallel(\mathcal{N}) \approx \frac{0.12}{\sqrt{\mathcal{N}}} \quad . \quad (43)$$

Other numerical estimates are given in section A.3. The angular resolution  $\Delta\beta_\perp$  as a function of  $\theta$ , is shown in Figure 14(a). The angular resolution  $\Delta\beta_\parallel$  as a function of  $\theta$ , is shown in Figure 14(b).

#### 6.11. $X_M$ resolution

The equation 5, defines the slant depth  $X(\ell)$  as a function of the coordinate along the EAS,  $\ell$ , and the atmospheric density,  $\rho(h(\ell))$ . Therefore one can derive an estimate of the angular resolution required to obtain any given  $X_M$  resolution by applying the

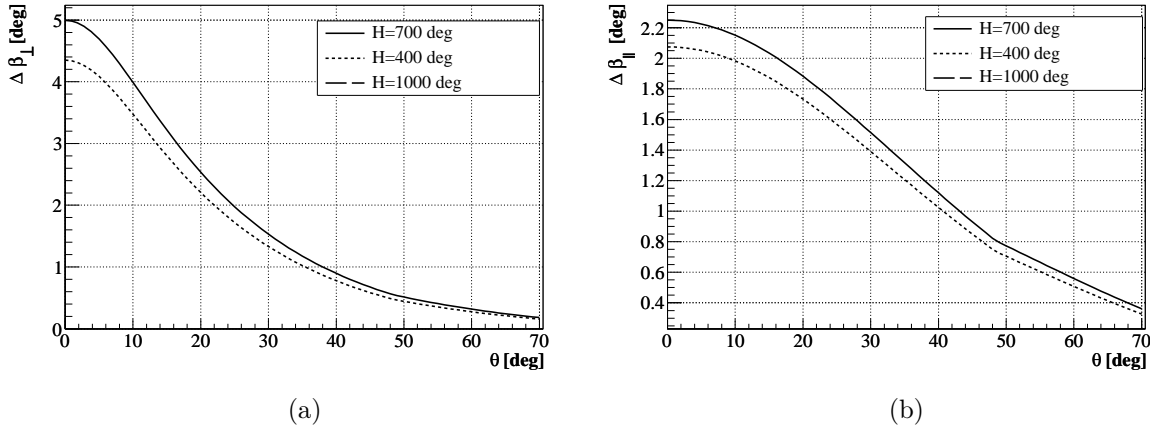


Figure 14. Angular resolution  $\Delta\beta_{\perp}$  (a) and  $\Delta\beta_{\parallel}$  (b) as a function of  $\theta$  in the reference conditions of Table 1. Solid line:  $H = 700$  km; dotted line:  $H = 400$  km (the line for  $H = 1000$  km is very close to the first one).  $\Delta\tau = 2.5 \mu\text{s}$ ,  $\Delta\alpha = 0.1^{\circ}$ .

equation at an altitude  $h \approx 6$  km, where the  $X_M$  of the reference EAS is located (see figure 5):

$$\Delta X \simeq \rho(h(\ell)) \Delta \ell \quad (44)$$

In the reference conditions of Table 1, it is  $\Delta \ell \approx 1.2$  km, for  $\Delta\alpha \sim 0.1^{\circ}$  (as determined in the previous section), so that:  $\Delta X_M \simeq 90 \text{ g/cm}^2$ . This shows that, in the reference conditions and neglecting the geometrical and kinematical details of the EAS development, one can estimate that in order to reach the required  $X_M$  resolution of  $\Delta X_M \simeq 50 \text{ g/cm}^2$  an angular granularity of the order of  $\Delta\alpha \sim 0.05^{\circ}$  is required.

### 6.12. Background and noise

A wide variety of background sources can affect the detection of UHECP from space. For every source the luminosity and variability in space and time must be studied and the data must be related to the local weather conditions.

Actually the sources of background to the EAS observation can be roughly divided into four main categories.

There are almost-continuous natural night sky diffuse and slowly varying sources, uniformly distributed in the FoV. The main component is the atmospheric night-glow [52]. Also the moon-reflected sunlight contributes significantly during the full moon time.

There are ground and man-made sources, localized in the FoV, such as city lights or other luminous sources slowly moving with respect to the satellite

speed projected on ground (airplanes, cars, ...). The sources of this class could blind the detector in the corresponding region of the FoV. The knowledge of their position in the FoV and their emission properties in the observational wavelength range will be helpful to limit their effect on the instrument duty cycle.

Transient Luminous Events (TLE) [53] in the lower atmosphere (lightnings) and in the upper atmosphere (red sprites, elves and blue jets) were discovered in the late eighties and are still poorly known. Recent measurements [54] have shown the existence of extremely powerful flashes in the near UV which may be related with the physics of the upper atmosphere. These luminous flashes might threaten the integrity of the photo-detector, if not properly taken into account. Therefore, the design of the orbit must optimize the duty cycle and minimize the aging effects, by avoiding the regions where the TLE are more frequent.

Finally there are other luminous events: satellites and debris in the sun light, meteorites, low energy cosmic radiation, satellite and satellite glow.

In this paper, looking for the minimal necessary requirements for the observation, only the continuous random background is taken into account, since it can be directly measured and subtracted. All the other background sources require a different handling and their space-time structure, distinct from the one of the EAS, must be exploited to reject them.

The total random background rate intercepted by the telescope (on the whole entrance pupil and full FoV) is:

$$\nu_{\text{tot}}^{\text{b}} = BA_{\text{EP}}\pi \sin^2 \gamma_{\text{M}} . \quad (45)$$

A typical value for the total rate of background hits detected is of the order of 10 THz. See Section A.4 for some numerical estimates.

The intrinsic noise generated by all the parts of the experimental telescope has to be kept well below the physical background level, due to the faintness of the air scintillation signal. It is therefore required to be less than a few GHz (over the whole photo-detector) in order to be negligible with respect to the background. Note that this requirement should also include the stray-light coming from lack of light-tightness of the telescope.

The online subtraction of the random background is mandatory as its rate is not negligible with respect to the rate of the air scintillation signal, especially for EAS near the energy threshold. A continuous monitoring of the average background on a pixel-by-pixel basis, is therefore unavoidable to subtract it and to lower the energy threshold.

Many experiments have measured the intensity of the random background from space: BABY [31], NIGHTGLOW [55], Arizona-Airglow [56] and the Universitetsky-Tatiana microsatellite [57]. However, in order to devise a method for online background subtraction, it is necessary to have a finer characterization of the space-time behavior of the background on the space-time scale of the EAS development:  $\Delta\alpha \simeq 0.1^\circ$  and  $\Delta t \simeq \mu\text{s}$ . This characterization should include measurements along different directions from nadir to cope with off-field background [14]. These measurements are relevant due to the large FoV, especially with a tilted telescope.

## 7. Conclusions

The design of a space-based telescope aimed at the observation of the EAS produced by UHECP is a very challenging task, particularly because of the small photon signal, the large photon background, the harsh space environment and the limited resources of a space mission. It is therefore very important to optimize the performance of the telescope, after defining the scientific requirements, and set safe design margins at the beginning of the concept study itself.

In this paper we have presented a set of analytical formulas and semi-analytical results that might be useful for the design of a future space-based experiment. These formulas and results allows one to set the approximate values of the design parameters,

starting from given scientific requirements. These design parameters can be refined, afterwards, with detailed, as well as heavy and time consuming, full Monte-Carlo simulations.

The formulas and results were used to estimate the expected performance of realistic satellite configuration, the sEUSO mission proposed to ESA in the framework of the Cosmic Vision program 2015-2025 [22].

We believe that before starting such a large and challenging free-flyer mission, a number of intermediate steps are needed, including preliminary measurements of the background and some sort of technology demonstrator. The envisaged JAXA JEM-EUSO [19] mission might well play the role of a pathfinder.

## Acknowledgments

The authors wish to thank the members of the EUSO Collaboration and in particular Osvaldo Catalano (INAF/IASF-Palermo), Didier Lebrun (LPSC, Grenoble), Piero Mazzinghi (INOA, Firenze), Sergio Bottai (INFN, Firenze) Andrea Santangelo (IAAAA, Tübingen), Dmitry Naumov (JINR, Dubna), Lloyd Hillman<sup>†</sup> (University of Alabama, Huntsville), Yoshi Takahashi<sup>†</sup> and John Linsley<sup>†</sup> for many useful discussions and suggestions.

The pioneering work [10] of Katsushi Arisaka (UCLA, Los Angeles) is acknowledged.

All this would have not been possible without the boost of Livio Scarsi<sup>†</sup>.

The many constructive comments/criticisms of two anonymous referees are acknowledged.

## Appendix A. Some order of magnitude estimates

### A.1. Air scintillation signal

Let us consider the reference conditions of Table 1 and an ideal telescope optics ( $\mathcal{E}'_O(\gamma) = A_{\text{EP}} \cos \gamma$ ).

The signal time-integrated irradiance reaching the telescope is given in Table A.1, for different values of  $\theta$  and  $H$ , the values of the other parameters being as in Table 1. Note that the irradiance scales as  $\sim (\cos \gamma/H)^2$ .

<sup>†</sup> Deceased.

$d\mathcal{N}/dA$ [ph·m <sup>-2</sup> ]	$\theta = 30^\circ$	$\theta = 50^\circ$	$\theta = 70^\circ$
$H = 400$ km	40	70	180
$H = 700$ km	15	25	60
$H = 1000$ km	5	10	30

Table A.1  
Signal time-integrated irradiance,  $d\mathcal{N}/dA$ , in the reference conditions of Table 1.

The detection of such an EAS obviously requires a large entrance pupil of many square meters, in order to get a number of detected photons of the order of a few hundreds as the total efficiency (optics, filters and photo-detector) is  $\varepsilon_{\text{tot}} \approx 0.1$ .

The typical angular length and the time duration of the EAS image are given respectively in Tables A.2 and A.3.

$\xi_{\text{EAS}}$ [deg]	$\theta = 30^\circ$	$\theta = 50^\circ$	$\theta = 70^\circ$
$H = 400$ km	0.8	1.7	3.1
$H = 700$ km	0.4	1.0	1.8
$H = 1000$ km	0.3	0.7	1.2

Table A.2  
Angular length  $\xi_{\text{EAS}}$  in the reference conditions of Table 1.

$T_{\text{EAS}}$ [ $\mu\text{s}$ ]	$\theta = 30^\circ$	$\theta = 50^\circ$	$\theta = 70^\circ$
$H = 400$ km	60	84	102
$H = 700$ km	60	84	103
$H = 1000$ km	60	84	104

Table A.3  
Time duration  $T_{\text{EAS}}$  in the reference conditions of Table 1.

## A.2. Requirements on the optical triggering efficacy

Following the discussion in Section 6.6, the required overall photo-detection efficacy in the reference conditions of Table 1 can be calculated

$$\mathcal{E}_{\text{tel}}(\gamma = 15^\circ) \approx \mathcal{N} \left( \frac{d\mathcal{N}}{dA} \right)^{-1},$$

where  $\mathcal{N} \simeq 100$  at the energy threshold. Using the values of the time-integrated irradiance given in the previous section it is  $\mathcal{E}_{\text{tel}}(\gamma = 15^\circ) \approx 4 \text{ m}^2$  when observing at  $H = 700$  km,  $\mathcal{E}_{\text{tel}}(\gamma = 15^\circ) \approx 1.5 \text{ m}^2$  at  $H = 400$  km and  $\mathcal{E}_{\text{tel}}(\gamma = 15^\circ) \approx 10 \text{ m}^2$  at  $H = 1000$  km.

Assuming conservatively  $\varepsilon_{\text{f}}\varepsilon_{\text{PD}} \sim 0.1$ , the optical triggering efficacy is obtained from the equation (24),

$$\mathcal{E}'_{\text{O}}(\gamma = 15^\circ) \approx \frac{\mathcal{E}_{\text{tel}}}{\varepsilon_{\text{f}}\varepsilon_{\text{PD}}} \approx \begin{cases} 15 \text{ m}^2 & \text{at } H = 400 \text{ km} \\ 40 \text{ m}^2 & \text{at } H = 700 \text{ km} \\ 100 \text{ m}^2 & \text{at } H = 1000 \text{ km} \end{cases} . \quad (\text{A.1})$$

The optical triggering efficacy at  $\gamma = 0^\circ$ , that is the entrance pupil area, is not only the effective photon collection area but it is also an estimate of the physical area of the optics, actually an optimistic one. Therefore it translates into a requirement on the minimum size of the telescope.

For an ideal optics, such that the optical triggering efficacy is  $\mathcal{E}'_{\text{O}}(\gamma) = A_{\text{EP}} \cos \gamma$ , it is

$$A_{\text{min}} \approx \frac{\mathcal{E}'_{\text{O}}(15^\circ)}{\cos 15^\circ} \approx \begin{cases} 16 \text{ m}^2 & \text{at } H = 400 \text{ km} \\ 42 \text{ m}^2 & \text{at } H = 700 \text{ km} \\ 104 \text{ m}^2 & \text{at } H = 1000 \text{ km} \end{cases} .$$

$$D_{\text{min}} \approx 2\sqrt{\frac{A_{\text{min}}}{\pi}} \approx \begin{cases} 4.5 \text{ m} & \text{at } H = 400 \text{ km} \\ 7.5 \text{ m} & \text{at } H = 700 \text{ km} \\ 12 \text{ m} & \text{at } H = 1000 \text{ km} \end{cases} . \quad (\text{A.2})$$

These results cannot be applied without accounting for the other sources of inefficiencies in a real optical system, so that the lower limit on  $D_{\text{min}}$  might increase by a factor, as confirmed by Monte-Carlo simulations [11,45,46].

## A.3. Granularity and angular resolution

Requiring a spatial granularity on Earth surface  $\Delta L \lesssim 1$  km, the required pixel granularity at different orbital heights can be fixed:

$$\Delta\alpha \approx \frac{\Delta L}{H} \approx \begin{cases} 0.10^\circ & \text{at } H = 400 \text{ km} \\ 0.06^\circ & \text{at } H = 700 \text{ km} \\ 0.04^\circ & \text{at } H = 1000 \text{ km} \end{cases} . \quad (\text{A.3})$$

Using the values of Table A.2 it turns out that the image of an EAS with  $\theta = 50^\circ$  is about 17 pixels long and there are about 6 photons per pixel on average.

The pixel size on the focal surface, from equation (14), is  $d \approx 5$  mm, using the minimum diameter from equation (A.2), and  $F_{\text{n}} \sim 0.5$ . This value of  $d$  does not depend on  $H$  since  $D_{\text{min}} \propto H$ .

It turns out that, in the reference conditions of Table 1, the angular resolution perpendicular



ular and parallel to the line-of-sight are both  $\sim 0.5^\circ$ . The total angular resolution is then  $\Delta\beta_{\text{tot}} = \sqrt{\Delta\beta_{\perp}^2 + \Delta\beta_{\parallel}^2} \lesssim 1^\circ$ .

#### A.4. The Random Background

The total random background rate intercepted on the whole entrance pupil by the telescope, in the reference conditions of Table 1, with  $\gamma_M = 20^\circ$  is given in Table A.4, together with the corresponding total number of pixels and the total random background rate per pixel (with a total efficiency  $\varepsilon_{\text{tot}} \approx 0.1$ ).

H	$N_{\text{pix}}$	$\nu_{\text{tot}}^{\text{b}}$	$\nu_{\text{pix}}^{\text{b}}$
[km]		[THz]	[MHz]
400	$1.2 \cdot 10^5$	2.8	2.3
700	$3.5 \cdot 10^5$	7.6	2.2
1000	$7.8 \cdot 10^5$	19.0	2.4

Table A.4

Number of pixels, total random background rate and background rate per pixel, in the reference conditions of Table 1. The values of  $A_{\text{EP}}$  and  $\Delta\alpha$  from equations (A.2) and (A.3), respectively, are used.

The results show that there is one order of magnitude more background than signal photons superimposed on the typical EAS (all space-time length) and roughly the same number of signal and random background photons near the EAS maximum.

## Appendix B. Estimation of the performance of sEUSO

The sEUSO mission [20] was proposed to ESA in the framework of the Cosmic Vision program 2015-2025 [22]. It is an enlarged and improved free-flyer version of the former EUSO mission [12], modifying several aspects and exploiting novel technologies. The design of the experimental telescope exploits the results of the detailed studies carried on during the phase A of EUSO [24] to redesign the telescope in such a way to fully satisfy the Scientific Requirements listed in Section 4.1.

The estimation of the performance of sEUSO is relative to EUSO [24]. It safely relies on the EUSO phase-A studies, based on full simulations, including the signal generation and transport, the telescope response as well as data analysis [11]. The EUSO performance is rescaled to the new telescope on the basis of simple approximate scaling laws

and/or consolidated expectations based on new technologies/techniques developments.

The optics efficiency can be improved by a factor  $\approx 1.5$  with respect to EUSO, by using a different, catadioptric, optical system with a slightly reduced FoV ( $\gamma_M = 20^\circ \div 25^\circ$ ). The instantaneous geometrical aperture is then recovered by means of higher altitude orbits.

The photo-detection efficiency can realistically improve by a factor  $\approx 3$  with respect to EUSO, thanks to newly developed photo-sensors with a larger quantum efficiency and a better flexibility in the design, which will allow to improve the filling factor of the focal surface.

As the entrance pupil size is the only parameter affecting the performance of the experiment whose size can be chosen, to within practical constraints, the telescope is designed to have the largest possible size compatible with a non-deployable photo-detector. In fact, while large deployable optical systems are under development for many other applications [58], the engineering of a deployable photo-detector does not appear as a realistic option. In order to cope with the very large optics required, a reflective deployable optical system is preferred. A reflective optical system has also the additional advantage to allow a smaller  $F_n$  than a refractive optical system, thus helping to limit the size of the focal surface. The  $F_n = 0.7$  is used. With all these assumption, the increase of the entrance pupil size can give a factor  $\approx 10$  improvement in the efficiency of the optics.

The three above factors give an overall  $\approx 45$  factor improvement in the photon collection capability.

The satellite orbit is an elliptical one, with the apogee in the range  $r_a \approx (800 \div 1200)$  km and the perigee as low as possible, compatibly with the constraints from the space mission, including atmospheric drag. The perigee is in the range  $r_p \approx (600 \div 1000)$  km. With a perigee twice larger than the EUSO one, there is still a factor  $\approx 45/4 = 11.25$  improvement with respect to EUSO in the overall photon detection capability. Since the EUSO efficiency as a function of the EAS energy reached a plateau at about  $E \approx 2 \cdot 10^{20}$  eV, (for EAS in the zenith angle range  $30^\circ < \theta < 70^\circ$ ), the energy threshold of sEUSO will be at  $E \approx 2 \cdot 10^{19}$  eV. Moreover, for EAS with zenith angle  $\theta > 60^\circ$ , the EUSO efficiency as a function of the EAS energy reached a plateau at  $E \approx 1 \cdot 10^{20}$  eV, so that sEUSO would have an energy threshold of  $E \approx 1 \cdot 10^{19}$  eV.

The EAS triggering and reconstruction efficiency

might be improved as well, by exploiting the larger number of photons with respect to EUSO, but this is not taken into account in the present analysis.

The result coming from all these assumptions lead to the parameters summarized in Table B.

## References

- [1] J. Abraham et al., Phys. Rev. Lett. 101 (2008) 061101.
- [2] D. Zavrtanik, Contemp. Phys. 51 (2010) 513–529.
- [3] A.A. Watson, Nucl. Instrum. Meth. A 588 (2008) 221–226.
- [4] J.N. Matthews et al., Nucl. Phys. Proc. Suppl. 212-213 (2011) 79. H. Tokuno et al., J. Phys. Conf. Ser. 293 (2011) 012035.
- [5] J. Abraham et al. Astropart. Phys. 29:188–204, 2008; Astropart. Phys. 31 (2009) 399; Phys. Rev. D 79 (2009) 102001; Astropart. Phys. 32 (2009) 89, [Erratum-ibid. 33 (2010) 65]; Phys. Lett. B 685 (2010) 239; Phys. Rev. Lett. 104 (2010) 091101; Astropart. Phys. 33 (2010) 108.
- [6] P. Abreu et al., Astropart. Phys. 34 (2010) 314–326; Astropart. Phys. 34 (2011) 627–639; JCAP 1106 (2011) 022.
- [7] R.U. Abbasi et al., Phys. Rev. Lett. 100 (2008) 101101.
- [8] M. Takeda et al., Phys. Rev. Lett. 81 (1998) 1163.
- [9] M. Pallavicini, R. Pesce, A. Petrolini and A. Thea, The observation of Extensive Air Showers from Space, arXiv:0810.5711 [astro-ph].
- [10] K. Arisaka, Optimization of an OWL-Airwatch Optics and Photo-Detectors (1999), [www.ge.infn.it/euso/docs/arisaka.pdf](http://www.ge.infn.it/euso/docs/arisaka.pdf).
- [11] C. Berat et al., Astropart. Phys. 33 (2010) 221.
- [12] J. Adams, Nucl. Phys. Proc. Suppl. 134 (2004) 15–22.
- [13] A. Petrolini, Nucl. Instr. Meth. A588 (2008) 201–206.
- [14] A. Thea et al, Nucl. Phys. B-Proc. Suppl. 166 (2006) 223–228.
- [15] A. Santangelo and A. Petrolini, New J. Phys. 11 (2009) 065010.
- [16] R. Benson and J. Linsley, *Satellite observation of cosmic ray air showers*, Proc. 17th ICRC (1981).
- [17] F.W. Stecker et al., Nucl. Phys. B-Proc. Suppl. 136C (2004) 433.
- [18] V.I. Abrashkin et al., Int. J. Mod. Phys., A20 (2005) 6865–6868.
- [19] Y. Takahashi et al., New Journal of Physics, Vol. 11, N. 065009, 2009
- [20] A. Santangelo, A. Petrolini, et al, S-EUSO: a proposal for a space-based observatory for UHECP, Technical report, 2007, [www.ge.infn.it/euso/docs/S-EUSO\\_Proposal.pdf](http://www.ge.infn.it/euso/docs/S-EUSO_Proposal.pdf).
- [21] A. Petrolini, Nucl. Instrum. Meth. A630 (2011) 131–135.
- [22] ESA, Cosmic Vision. Space Science for Europe 2015-2025, 2005, <http://www.esa.int/esapub/br/br247/br247.pdf>.
- [23] I.F.M. Albuquerque and G.F. Smoot, Astropart. Phys. 25 (2006) 375.
- [24] The EUSO Collaboration. EUSO: Report on the Phase A Study, Internal note EUSO-PI-REP-002 (2003), <http://www.ge.infn.it/euso/docs/EUSO-PI-REP-002.pdf>.
- [25] US Standard Atmosphere [http://modelweb.gsfc.nasa.gov/atmos/us\\_standard.html](http://modelweb.gsfc.nasa.gov/atmos/us_standard.html).
- [26] A.N. Cox (ed.), Allen’s Astrophysical Quantities. AIP Press, 1999.
- [27] T. K. Gaisser and A. M. Hillas, Proc. 15th ICRC 8 (1977) 353.
- [28] C. Pryke, Astropart. Phys. 14 (2001) 319–328.
- [29] T. Stanev, High Energy Cosmic Rays. Springer, 2004.
- [30] T. Bergmann et al., Astropart. Phys. 26 (2007) 420.
- [31] O. Catalano et al., Nucl. Instrum. Methods A 480 (2002) 547–554.
- [32] F. Kakimoto et al., Nucl. Instrum. Meth. A 372 (1996) 527–533.
- [33] M. Nagano et al., Astropart. Phys. 22 (2004) 235–248.
- [34] R. Abbasi et al., Astropart. Phys. 29 (2008) 77.
- [35] M. Ave et al., Nucl. Phys. Proc. Suppl. 212-213 (2011) 356-361.
- [36] A. Bucholtz, Appl. Optics 34(15) (1995) 2765–2773.
- [37] A. T. Young, Appl. Optics 33(6) (1994) 1108–1110.
- [38] P. Grieder, *Cosmic rays at Earth*, Elsevier, 2001.
- [39] P. Sokolsky and J. Krizmanic, Astropart. Phys. 20 (2004) 391.
- [40] T. Abu-Zayyad, C.C.H. Jui and E.C. Loh, Astropart. Phys. 21 (2004) 163.
- [41] J. Wertz and W. Larson (eds.), Space missions analysis and design, Microcosm Press, 1999.
- [42] P. Mazzinghi et al, Physics and Astrophysics in Space (Frascati Physics Series) vol. xxxvii (2004) 437-444.
- [43] T. Gys, Nucl. Instrum. Meth. A 595 (2008) 136. M. Suyama and K. Nakamura, *Recent progress of photocathodes for PMTs*, [http://pos.sissa.it/archive/conferences/090/013/PD09\\_013.pdf](http://pos.sissa.it/archive/conferences/090/013/PD09_013.pdf);
- [44] K. Nakamura, Y. Hamana, Y. Ishigami and T. Matsui, Nucl. Instrum. Meth. A 623 (2010) 276. T. Iijima, Nucl. Instrum. Meth. A 639 (2011) 137.
- [45] R. Chechik and A. Breskin, Nucl. Instrum. Meth. A 595 (2008) 116. J. Haba, Nucl. Instrum. Meth. A 595 (2008) 154. Nucl. Instrum. Meth. A 610 (2009) 1–450; *New Developments In Photodetection*, NDIP11, Proceedings of the 6th International Conference on New Developments in Photodetection. S. Korpar, Nucl. Instrum. Meth. A 639 (2011) 88. S. Dalla Torre, Nucl. Instrum. Meth. A 639 (2011) 111.
- [46] A. Thea, Observation of UHECR from space. PhD thesis, Università degli Studi di Genova, 2006, [http://www.ge.infn.it/euso/docs/AThea\\_PhDThesis.pdf](http://www.ge.infn.it/euso/docs/AThea_PhDThesis.pdf).
- [47] R. Pesce, The observation of UHECP on the Earth and from space, PhD thesis, Università degli Studi di Genova, 2008, [http://www.ge.infn.it/euso/docs/RPesce\\_PhDThesis.pdf](http://www.ge.infn.it/euso/docs/RPesce_PhDThesis.pdf).
- [48] M.G. Kendall, A. Stuart, J.K. Ord and S. Arnold, *Kendall’s advanced theory of statistics*, Griffin, 2004.
- [49] C. Berat et al., Proc. 28th ICRC (2003) 927–930.
- [50] A. Petrolini, *Least-squares fit to a straight line when each variable contains all equal errors*, arXiv:1104.3132 [physics.data-an].
- [51] P. Sommers, Astropart. Phys. 3 (1995) 349–360.
- [52] R. M. Baltrusaitis et al., Nucl. Instrum. Meth. A 240 (1985) 410–428.
- [53] R.R. Meier, Space Science Reviews 58(1) (1991) 1–185.
- [54] U.S. Inan et al., Geophys. Res. Lett. 18 (1991) 705–708.
- [55] G.K. Garipov et al., Astropart. Phys. 24 (2005) 400–408.

Satellite and Orbit		
Orbit perigee	$r_p \approx 800$ km	$r_p \approx (600 \div 1000)$ km
Orbit apogee	$r_a \approx 1100$ km	$r_a \approx (800 \div 1200)$ km
Orbit inclination	$i \approx 50^\circ \div 60^\circ$	preferred
Orbital period	$T \approx 100$ min	
Pointing and pointing accuracy	nadir to within $3^\circ$	must be known offline to within $0.5^\circ$
Lifetime	$> 5$ years	10 years goal
Telescope		
Type	deployable catadioptric system	
Main mirror diameter	$D_M = 11$ m	
Entrance pupil diameter	$D_{EP} = 7$ m	
Field of View	$\gamma_M = 25^\circ$	half-angle
Angular granularity	$\Delta\alpha \approx 0.04^\circ$	
Linear granularity	$\Delta L \approx 0.7$ km at Earth	average
Optical triggering efficacy	$\mathcal{E}'_O \gtrsim 108$ m <sup>2</sup>	average requirement
f-number	$F_n \approx 0.7$	current design (goal: $F_n \approx 0.6$ )
Focal surface diameter	$D_{PD} = 4$ m	
Photo-detection efficiency	$\varepsilon_{PD} \gtrsim 0.25$	average requirement
Number of pixels	$N_{\text{pix}} \approx 1.2 \cdot 10^6$	
Pixel size	$\delta \approx 4$ mm	to be optimized
Performance		
Energy threshold	$E_{\text{th}} \approx 1 \cdot 10^{19}$ eV	
Instantaneous geometrical aperture	$\mathcal{A}_g \approx 2 \cdot 10^6$ km <sup>2</sup> ·sr	
Statistical error on the energy	$\Delta E / E \approx 0.1$ at $E = 1 \cdot 10^{19}$ eV	requirement
Angular resolution	$\Delta\beta \lesssim 3^\circ$	depends on the EAS direction
Observational duty cycle	$\eta_o \approx 0.1 \div 0.2$	dedicated measurements required

Table B.1

Main baseline parameters of the sEUSO mission.

- [55] L.M. Barbier et al., *Astropart. Phys.* 22 (2005) 439–449.
- [56] D.J. Knecht et al., *Adv. Space Res.*, 19(4) (1997) 627–630.
- [57] G.K. Garipov et al., *JETP Lett.*, 82(4) (2005) 185–187.
- [58] A. Zuccaro Marchi et al., *Technological Developments for Ultra-Lightweight, Large Aperture, Deployable Mirror for Space Telescopes*, International Conference on Space Optics, ICSO 2010.